Exploring the spatial relationship between airborne-derived red and far-red sun-induced fluorescence and process-based GPP estimates in a forest ecosystem

Giulia Tagliabue[1,*], Cinzia Panigada[1], Benjamin Dechant[2], Frédéric Baret[3], Sergio Cogliati[1], Roberto Colombo[1], Mirco Migliavacca[4], Patrick Rademske[5], Anke Schickling[5], Dirk Schüttemeyer[6], Jochem Verrelst[7], Uwe Rascher[5], Youngryel Ryu[2], Micol Rossini[1]

[1]Remote Sensing of Environmental Dynamics Laboratory, Department of Environmental and Earth Sciences, University of Milano-Bicocca, Italy; [2]Department of Landscape Architecture and Rural Systems Engineering, Seoul National University, South Korea; [3]Institut National de la Recherche Agronomique, France; [4]Max Planck Institute for Biogeochemistry, Germany; [5]Institute of Bio- and Geosciences, IBG-2 Plant Sciences, Forschungszentrum Jülich GmbH, Germany; [6]European Space Agency, The Netherlands; [7]Image Processing Laboratory, University of Valencia, Spain. *Corresponding Author

Abstract

Terrestrial gross primary productivity plays an essential role in the global carbon cycle, but the quantification of the spatial and temporal variations in photosynthesis is still largely uncertain. Our work aimed at investigating the potential of remote sensing to provide new insights into the plant actual photosynthesis at fine spatial resolution. This was achieved exploiting high-resolution images acquired with the FLEX airborne demonstrator *HyPlant*. The sensor was flown over a mixed forest and the images collected were elaborated to obtain two independent estimates of plant photosynthesis. Firstly, maps of sun-induced chlorophyll fluorescence (F), a novel indicator of plant photosynthetic activity, were successfully obtained at both the red and far-red peak (r^2=0.74, $p<0.001$ and r^2=0.73, $p<0.001$, respectively, compared to top-of-canopy ground-based measurements acquired synchronously with the overflight) over the forested study area. Secondly, maps of gross primary productivity (GPP) and absorbed photosynthetically active radiation (APAR) were derived using a customised version of the coupled biophysical model Breathing Earth System Simulator (BESS). The model driven with airborne-derived maps of key forest traits (i.e., leaf chlorophyll content (LCC) and leaf area index (LAI)) and meteorological data provided a high-resolution snapshot of the

variables of interest across the study site. LCC and LAI were accurately estimated (RMSE=5.66 μg cm^{-2} and RMSE=0.51 m^2 m^{-2}, respectively) through an optimised Look-Up-Table based inversion of the PROSPECT-4-INFORM radiative transfer model, ensuring the accurate representation of the spatial variation of these determinants of the ecosystem's functionality. The spatial relationships between measured F and modelled BESS outputs were then analysed to interpret the variability of ecosystem functioning at regional scale. Results showed that far-red F is significantly correlated with GPP (r^2=0.46, $p<0.001$) and APAR (r^2=0.43, $p<0.001$) in the spatial domain, and that this relationship is nonlinear. Conversely, no statistically significant relationships were found between red F and GPP or red F and APAR ($p>0.05$). The spatial relationships found at high resolution constitute a valuable insight into the critical role of the spatial heterogeneity in controlling the carbon uptake, entailing the need to take it into account at coarser resolution.

Keywords: Sun-induced chlorophyll fluorescence; Spectral fitting method; Plant traits; INFORM; GPP; APAR; LUE; BESS; Forest ecosystems; HyPlant; Airborne spectroscopy.

1. Introduction

Photosynthesis is the primary process supporting life on Earth. Terrestrial plants exchange CO_2 with the atmosphere through this process, thereby playing a major role within the global carbon cycle (Beer et al. 2010; Heimann & Reichstein 2008). The carbon sequestration capacity is the result of complex and interconnected dynamics that counterpose in a delicate balance (Schimel 1995; Cao et al. 1998). Global change is altering this balance, with consequences on the functioning of the Earth system (Ciais et al. 2013 in IPCC, 2013; Zhu et al. 2016). This is fostering the quantification of the exact magnitude of these processes, which is nowadays still largely unknown (Schimel et al. 2015; Heimann & Reichstein 2008).

Recent advances in remote sensing of sun-induced chlorophyll fluorescence (F) disclosed unprecedented opportunities in the large-scale monitoring of terrestrial vegetation. F is a faint electromagnetic signal emitted in the red and far-red spectral regions (i.e., 650-800 nm) by the core of the photosynthetic machinery to dissipate the excess of absorbed solar radiation (Papageorgiu & Govindjee 2004). Photochemistry competes with heat dissipation and F emission for the absorbed radiation. Therefore, measurements of

energy de-excitation pathways (i.e., fluorescence and heat dissipation) are expected to provide an indirect assessment of photochemical efficiency (Baker et al. 2008). This link constitutes the rationale behind the use of F to infer the actual functional status of the photosynthetic machinery.

Although there is solid evidence of this relationship at sub-cellular to leaf scale due to considerable efforts undertaken until now using active fluorescence techniques (Baker et al. 2008; Porcar-Castell et al. 2014; Genty et al. 1989), the relationship between passive fluorescence and photosynthesis at the canopy scale is still hazy and largely unknown. Lately, various studies showed strong empirical linear relationships (even though in some cases biome dependent) between F and gross primary productivity (GPP) (i.e., measure of terrestrial apparent photosynthesis (Wohlfahrt & Gu 2015)) at coarse spatial scales (e.g., Sun et al. 2017; Li et al. 2018; Yang et al. 2015; Frankenberg et al. 2011; Guanter et al. 2012), but several knowledge gaps still exist. Actually, the majority of the studies is based on the exploitation of space-based retrievals of F from high spectral resolution spectrometers onboard satellites deployed for atmospheric studies (e.g., Global Ozone Monitoring Experiment 2 (GOME-2) (Munro et al. 2016); TANSO Fourier Transform Spectrometer (Hamazaki et al. 2004), Orbiting Carbon Observatory-2 (Frankenberg et al. 2015). These sensors opened the possibility to observe F from space but their coarse spatial resolution - from 2 km to 80 km - and in some cases sparse spatial sampling is unsuitable to capture the heterogeneity of terrestrial ecosystems. This aspect strongly limited the investigation of the spatial variability of F and GPP.

GPP is the most direct available proxy of photosynthesis, but the uncertainties related to its modelling at the global scale hamper an accurate quantification of the imprint of plants on the carbon cycle. Current models for the quantification of terrestrial GPP (e.g., Tramontana et al. 2016; Jung et al. 2011; Beer et al. 2010; Ryu et al. 2011; van der Tol et al. 2009; Knorr 2000) are characterised by an advanced process understanding. However, uncertainties in the carbon flux modelling come from the structure of the model employed, the quality of the meteorological forcings and most importantly the adequacy of the model parameterisation. Regardless of the typology (i.e. data-driven or process-based model), the effectiveness of these models is in fact severely conditioned by the accuracy of the input parameters (Jung et al. 2007; Friedlingstein et al. 2014; Houborg et al. 2015a), that vary across space and over time (Rogers et al. 2017).

77 The bridge to fill this gap is represented by the incorporation in the models of accurate spatially and
78 temporally resolved plant trait-related information. As a matter of fact, the variability of plant traits (e.g. leaf
79 chlorophyll content (LCC), leaf area index (LAI)) constitutes a determinant of the functionality of the
80 ecosystem, that must be taken into account to constrain the flux estimation (Butler et al. 2017; van Bodegom
81 et al. 2014; van Bodegom et al. 2012). This aspect, though extremely relevant, was mostly neglected in
82 previous studies because of the lack of adequate spatio-temporal data. The increasing availability of remote
83 sensing (RS) observations might overcome this limitation, as RS can provide repeated spatially-distributed
84 plant trait-related information (Schimel et al. 2015, Homolova et al. 2013).
85 The retrieval of plant traits from RS observations advanced significantly over the last decades due to a
86 considerable effort posed in the development and testing of multiple retrieval methods (for a review, see
87 Verrelst et al. 2015a, 2018). Among the retrieval algorithms, the inversion of physically-based radiative
88 transfer models (RTMs) is generally considered a reliable approach (Atzberger et al. 2015; Dorigo et al. 2007).
89 RTMs exploit physical laws to describe the interactions between the incident solar radiation and the
90 vegetation medium. Being founded on a physical relationship between measured radiometric signal and
91 plant traits, the inversion of these models constitutes an accurate, robust and generic approach for plant trait
92 retrievals (Verrelst et al. 2015b; Atzberger et al. 2015; Houborg et al. 2015a; Dorigo et al. 2007).
93 Regardless of the progresses achieved, the retrieval of plant traits remains challenging. Their quantitative
94 estimation is hampered by the influence of various confounding factors (Wang et al. 2018; Zarco-Tejada et al.
95 2004). In physically-based frameworks, the main challenge is represented by the regularisation of the
96 undetermined and ill-posed nature of the inverse problem (Houborg et al. 2015a). Multiple combinations of
97 plant traits might yield analogous simulated spectra, resulting in non-unique solutions. Furthermore, the
98 uncertainties affecting both the model and the data may be source of large inaccuracies in the modelled
99 reflectance (Houborg et al. 2015a; Combal et al. 2002; Baret & Buis 2008). Hence, adequate model
100 parameterisation and regularisation strategies are critical to mitigate the drawbacks of ill-posedness and
101 obtain trustworthy results (Verrelst et al. 2014, 2015b; Houborg et al. 2015b; Combal et al. 2002). Several
102 studies recognised the importance of using prior information to reduce the variability of the input

parameters (e.g., Meroni et al. 2004; Malenovský et al. 2006; Baret & Buis 2008; Darvishzadeh et al. 2008), of adding noise to the simulated spectra (e.g., Kötz et al. 2005; Richter et al. 2009) and of using multiple solutions of the inversion (e.g., Combal et al. 2002; Kötz et al. 2005, Atzberger & Richter 2012). Conversely, the impact of using alternative cost functions to match simulated and measured reflectance has been poorly investigated (Rivera et al. 2013; Verrelst et al. 2014).

In this framework, this work aimed at investigating the potential of RS to provide new insights into the actual plant photosynthesis. High-resolution airborne hyperspectral images acquired with the *HyPlant* sensor (Rascher et al. 2015) over a mixed forest were used to provide two independent estimates of plant photosynthesis: red and far-red F on the one hand, GPP on the other. This comprehensive high-resolution analysis was made possible by the characteristics of the sensor, deployed as airborne demonstrator of the forthcoming FLuorescence EXplorer (FLEX) satellite (Drusch et al 2017): *HyPlant* was in fact specifically designed to acquire simultaneously sub-nanometric spectral information in the 650-800 nm spectral region and hyperspectral information between 400 and 2500 nm, providing the means to retrieve F as well as obtain hyperspectral reflectance.

We explored the possibility to: i) obtain high resolution ground-validated maps of both red and far-red F from airborne ultra-fine spectral resolution imagery using the spectral fitting method (SFM) (Cogliati et al. 2015); ii) obtain high resolution ground-validated maps of key forest traits (i.e., LCC and LAI) from airborne hyperspectral imagery through an optimised RTM inversion; iii) obtain high resolution maps of GPP, absorbed photosynthetically active radiation (APAR) and light use efficiency (LUE) through a modelling approach based on the use of the aforementioned airborne-derived spatially resolved traits to drive the Breathing Earth System Simulator (BESS) (Ryu et al. 2011; Jiang & Ryu 2016), a process-based ecophysiological model; with the ultimate goal of iv) exploring the spatial relationship existing between measured F and modelled BESS outputs at high resolution, in order to interpret the variability of ecosystem functioning at regional scale.

2 Material and methods

2.1 Study site

The study was conducted on a mid-latitude plain mixed forest (Hardt Forest) located in France (47°48'29" N, 7°26'53" E; Mulhouse; Alsace). The analysis focused on an area of ~90 ha located in the northern part of the forest, corresponding to a subset of the total area covered by the airborne overpasses (**Fig. 1**).

The climate of the region is temperate, with an average temperature of 22°C in summer and of 4°C in winter. The mean annual rainfall is 680 mm distributed throughout the year, with a prevalence between May and August.

The forest covers ~13 000 ha and is relatively managed, with stands of at least 500 m size characterised by a relatively large variability in terms of forest age. Overall, the fraction of deciduous and coniferous tree species is about 90% and 10%, respectively. The dominant canopy layer is characterised by the presence of European hornbeam (*Carpinus betulus* L.), pedunculate and sessile oak (*Quercus robur* L., *Quercus petraea* (Matt.) Liebl.), field maple (*Acer campestre* L.), small-leaved linden (*Tilia cordata* Mill.), Scots pine (*Pinus sylvestris* L.) and European larch (*Larix decidua* Mill.).

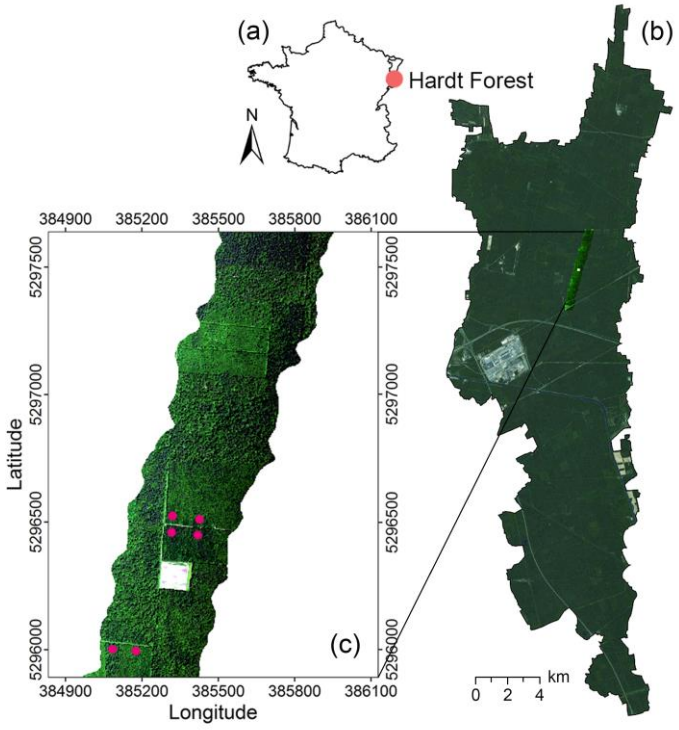

142 **Figure 1. a) Location of the Hardt Forest in Alsace, France; b) Hardt Forest and location of the *HyPlant***
143 **flightline used in this study (RGB true colour composite); c) Zoom of the *HyPlant* image and location of**
144 **the sites where top-of-canopy spectral measurements were collected (purple dots).**

145 **2.2 Field spectral measurements and plant traits data collection**

146 A field campaign was conducted in the summer of 2013 in order to collect spectral measurements, plant
147 traits and ancillary meteorological data.

148 Top-of-canopy high resolution radiance measurements were acquired on June 16th-17th and July 2nd, 2013
149 around midday (10:00-15:00 a.m. solar time) in clear-sky conditions using portable spectroradiometers
150 operating in the visible and near-infrared regions. The set-up included three different instruments (HR4000,
151 HR4000, QE65000; Ocean Optics, Dunedin, USA) characterised by different spectral ranges and resolutions:
152 the first one covering the spectral range 350-1050 nm with a full width at half maximum (FWHM) of 1 nm for
153 reflectance and vegetation indices computation; the second (spectral range 700-800 nm, FWHM=0.1 nm) and
154 third (spectral range 657-740 nm, FWHM=0.25 nm) ones specifically designed for the retrieval of sun-
155 induced chlorophyll fluorescence at the O_2-B (F_{687}) and O_2-A (F_{760}) absorption bands, respectively.

156 The system was housed in a thermally regulated Peltier box (model NT-16; Magapor, Zaragoza, Spain)
157 and manually operated from the top of a mobile hydraulic platform to measure top-of-canopy reflectance
158 and fluorescence of the representative tree species of the Hardt forest in six sampling sites. The
159 measurements were acquired from nadir using bare optical fibers with an angular field of view of 25°
160 mounted at the end of a 2.5 m long arm held at 3.7-5 m height from the canopy, corresponding to a sampling
161 area of 1.7-2.3 m diameter. The arm was manually rotated horizontally to allow observing either the
162 vegetated target to measure the upwelling radiance or a levelled calibrated white reference panel
163 (Spectralon; Labsphere, North Sutton, USA) to measure the incident solar radiation.

164 The spectral data were acquired through the 3S software (Meroni & Colombo 2009), sandwiching each
165 measurement of the vegetated target between two measurements of the white reference panel, and collecting
166 the dark current of the instruments at the beginning of each set of measurements. The collected data were
167 processed with a dedicated IDL (ITT Visual Information Solutions, Boulder, USA) application described in

168 Meroni et al. (2011). F_{687} and F_{760} were estimated by exploiting the spectral fitting method described in
169 Meroni et al. (2010) and Cogliati et al. (2015).

170 Field measurements were acquired in correspondence of Elementary Sampling Units (ESUs) of 20 x 20 m
171 distributed all over the study area in order to sample a wide range of different forest species and conditions.
172 The ESUs were selected by forest experts along the forest tracks, at about 50 m distance from the path. The
173 centre of each ESU was tracked with a high precision Trimble Geo-XT GPS (Trimble, Sunnyvale, USA).
174 Species composition and crown condition were visually evaluated by the forest experts in correspondence of
175 42 ESUs. All the species representing more than 5% of the dominant layer of the ESU were considered in the
176 estimation of the species composition. LCC was estimated by destructive measurements on leaves collected
177 from different forest species located in 12 ESUs. At least 10 leaves were sampled for each species of the ESUs
178 (n≈250). The leaf samples were collected from sunlit leaves sampled by shooting with guns at the top
179 branches and were immediately put into plastic bags, sealed, labelled and stored under -80°C until the
180 laboratory biochemical analysis. The pigments were extracted using hydroxide carbonate magnesium
181 buffered with acetone and absorbance was measured at 645, 662 and 710 nm using a UVIKON XL
182 spectrophotometer (BioTek Instruments, Winooski, USA) to determine LCC (Lichtenthaler & Buschmann
183 2001). LAI was estimated by means of digital hemispherical photos acquired in correspondence of 14 ESUs
184 using a Sigma camera (Sigma Corporation, Ronkonkoma, USA) equipped with a fisheye lens. The images - 7
185 looking upward per each plot - were processed with the CAN-EYE (https://www4.paca.inra.fr/can-
186 eye/CAN-EYE-Home/Welcome) software to estimate LAI. The clumping effect was taken into account by
187 multiplying the effective LAI by a coefficient, the clumping index (Chen & Black 1992), computed using the
188 logarithm gap fraction averaging method (Lang & Yueqin 1986).

189 **2.3 Airborne hyperspectral images acquisition and pre-processing**

190 The airborne data were acquired using the hyperspectral imaging sensor *HyPlant* (Rascher et al. 2015).
191 *HyPlant* is made up of two modules: i) the Dual Channel Imager (DUAL) is a hyperspectral imaging
192 spectrometer with up to 624 spectral channels covering the visible, near-infrared and shortwave infrared
193 (VIS-NIR-SWIR) spectral regions (370-2500 nm) at a full-width at half maximum (FWHM) of 4.0 (VIS-NIR) -

13.3 (SWIR) nm; ii) the Fluorescence Imager (FLUO) is a high-performance hyperspectral imaging spectrometer with up to 1024 spectral channels which provides contiguous spectral information in the wavelength range 670-780 nm with a FWHM of ~0.25 nm. Both the DUAL and FLUO sensors are line-imaging push-broom scanners with an angular field of view of 32.3°.

HyPlant was flown over the study site on board a Cessna Grand Caravan C208B on June 16, 2013 around solar noon (12:30±1 CEST (Central European Summer Time)) under clear sky conditions. The flight was conducted heading 195° at an average altitude of 600 m above the ground level, resulting in a pixel size of 1 m.

The pre-processing of the airborne data was performed using the CaliGeo software (Specim Ltd, Oulu, Finland). *HyPlant* raw data were corrected for dark current, radiometrically calibrated and georectified using as input the information recorded by *HyPlant* position and attitude sensor. The DUAL data were then atmospherically corrected using the ATCOR-4 atmospheric radiative transfer code to obtain top-of-canopy radiance and reflectance.

2.4 *HyPlant* data product generation

2.4.1 Sun-induced chlorophyll fluorescence retrieval

The images collected by the FLUO module were processed with a dedicated processing-chain specifically developed to retrieve F from *HyPlant* observations. The SFM retrieval approach, originally developed for FLEX (Cogliati et al. 2015), was adapted to *HyPlant* ultra-fine resolution data at both the O_2-B and O_2-A absorption bands to derive red and far-red F maps (Cogliati et al. 2018). This approach allowed decoupling F and surface reflected radiance spectra from upward radiance spectra detected by the *HyPlant* FLUO module. The rationale behind the SFM relies on mathematical functions to model canopy reflectance and fluorescence spectra at the different wavelengths. The exploitation of the full set of spectral bands provided by *HyPlant* sensor reduces the overall impact of instrumental noise and allows estimating a higher number of model parameters describing the fluorescence/reflectance spectra. The SFM method was implemented and tested for processing *HyPlant* images collected during the campaign, following the surface-atmosphere coupled RT scheme proposed in Verhoef et al. (2018) and adapted to airborne observations. In fact, reflectance and

fluorescence spectral function parameters were directly estimated comparing forward RT model simulations with *HyPlant* radiance spectra at-sensor level. The forward RT model used for processing *HyPlant* images was limited to estimating surface parameters (i.e. reflectance and fluorescence), while the atmospheric variables were kept constant to pre-defined values. The atmospheric transfer functions (i.e. path radiance, spherical albedo and upward/downward transmittance) used in the forward RT model were computed by MODTRAN5. The atmospheric model input parameters were derived from sunphotometer measurements collected simultaneously to *HyPlant* observations. The retrieval algorithm included a preliminary characterisation of instrumental signal distortions such as spectral-shift and bandwidth on image column base (i.e., sensor across-track). The red and far-red F at the O_2-A and O_2-B bands, respectively, were estimated by analysing each O_2 absorption band independently. The output of the SFM consists of two distinct images, in which the red (684-697 nm) and far-red (750-777 nm) F spectra (with a spectral sampling interval resampled to 1 nm in order to reduce the output data volume) are provided in physical units (mW m^{-2} sr^{-1} nm^{-1}). For further analysis, the F values at 687 nm (F_{687}) and 760 nm (F_{760}) were used in this study.

The maps were finally validated comparing the airborne with the ground-based retrievals obtained from top-of-canopy spectral measurements collected over six selected forest targets. The ground targets were precisely identified on the image with the help of RGB images acquired with a drone and statistics were extracted from regions of interest of 3 × 3 pixels for comparison against the ground-based measurements.

The fluorescence yields (Fy_{687} and Fy_{760}) were calculated as the ratio between F_{687} and F_{760} and APAR (μmol m^{-2} s^{-1}) for each pixel of the image. Before the calculation, F_{687} and F_{760} radiances were converted to irradiances multiplying by π and to μmol m^{-2} s^{-1} nm^{-1} using a specific wavelength-dependent coefficient. The resulting Fy_{687} and Fy_{760} maps refer to the emission at 687 and 760 nm, respectively, and are thus expressed as nm^{-1}.

2.4.2 Plant traits retrieval

In order to obtain accurate high-resolution maps of key plant traits from *HyPlant* DUAL imagery, a physically based approach was chosen. A systematic evaluation of the RTM parameterisation and of the LUT-based inversion strategy was conducted, in order to propose a reproducible approach that could

provide accurate and reliable plant trait retrievals in forest ecosystems, to be used for different purposes. In this case, the inversion strategy was optimised on the retrieval of LCC and LAI, two key traits for the following modelling step using BESS.

Among the variety of existing RTMs, the canopy level INvertible FOrest Reflectance Model (INFORM) (Atzberger 2000; Schlerf & Atzberger 2006) coupled with the leaf level PROSPECT-4 model (Jacquemoud & Baret 1990; Feret et al. 2008) was chosen in this study because of its suitability in simulating forest canopy reflectance while preserving a relative simplicity. INFORM is a hybrid model combining the strengths of the turbid-medium and geometric-optical radiative transfer models. It couples the SAILH model (Verhoef 1984; Kuusk 1991) that simulates the radiative transfer within the turbid-medium canopy layer with the FLIM model (Rosema 1992) to account for geometric aspects such as the leaf clumping inside the tree crowns and the crown geometry. The model simulates the forest reflectance in the spectral range 400-2500 nm as a function of several leaf-level (i.e., leaf chlorophyll content, leaf dry matter content, leaf water content, leaf structural parameter) as well as canopy-level (i.e., LAI of the single trees, LAI of the understory, average leaf angle, tree height, crown diameter, stem density) input parameters, besides other parameters describing the sun-sensor geometries and irradiance conditions (i.e., sun zenith angle, observer zenith angle, relative azimuth angle, fraction of diffuse radiation).

A global sensitivity analysis (GSA) (Saltelli 2010; Verrelst et al. 2015c) was carried out in order to examine the response of the model to the variation of each of its input parameters. This allows to identify the parameters that are less-influential on the modelled reflectance, that can be thereafter set to fixed values in order to reduce the number of unknown variables maximising the predictive power of the model. A total of 2000 simulations were run, varying each parameter according to all the possible variability in the study site. The GSA results were used to improve the parameterisation of the RTM: the less influential parameters on the modelled reflectance were set to constant values, while the other input parameters were varied within ranges defined according to prior knowledge of the study site. The range and distribution of the RTM input parameters used for the generation of the LUT are shown in **Table I**.

Table I. Range and distribution of the input parameters of the PROSPECT-4-INFORM model used for the generation of the LUT. (*μ=mean, σ=standard deviation)

	Variable		Unit	Range	Distribution
Prospect-4	LCC	Leaf chlorophyll content	μg cm^{-2}	10-70	Gaussian (*μ=40, σ=25)
	Cw	Leaf water content	cm	0.006-0.015	Sobol
	Cm	Dry matter content	g cm^2	0.003-0.015	Sobol
	N	Leaf structural parameter	-	1.5	-
Inform	LAI	Leaf area index	m^2 m^{-2}	1.5-8	Gaussian (μ=4, σ=2)
	LAIu	Leaf area index of understory	m^2 m^{-2}	0.5-2.5	Sobol
	sd	Stem density	trees ha^{-1}	200-400	Sobol
	cd	Crown diameter	m	3-9	Sobol
	h	Tree height	m	20	-
	ala	Average leaf inclination	deg	45	-
	θ_s	Sun zenith angle	deg	31	-
	θ_o	Observer zenith angle	deg	0	-
	Φ	Azimuth angle	deg	128	-
	skyl	Fraction of diffuse radiation	-	0.1	-

The model was then run in forward mode to generate a LUT of 30,000 simulated reflectance spectra obtained by all the possible combinations between the input parameters.

The inversion strategy was optimised by testing the effect of three regularisation options on the retrieval performances: i) the use of different cost functions, ii) the addition of Gaussian noise to the simulated spectra and iii) the use of multiple solutions of the inversion.

Multiple cost functions introduced in Leonenko et al. (2013) and exploited in Rivera et al. (2013) were tested, in order to identify the ones that minimise the mismatch between measured and simulated spectra. The cost functions belong to different fields of mathematics and statistics and can be grouped into three broad families: information measures, M-estimates and minimum contrast estimates.

All these metrics are used to minimise the distance $D[M,S]$ between two functions $M=(m(\lambda_1), m(\lambda_2), \ldots, m(\lambda_n))$ and $S=(s(\lambda_1), s(\lambda_2), \ldots, s(\lambda_n))$, representing the shape of the measured (M) and simulated (S) reflectance spectra at the wavelength λ_n, but different metrics describe D in distinctive ways.

With the information measures (e.g., Kullback Leibler divergence, Pearson chi-square, harmonique Toussaint measure), M and S are considered as probability distributions and their divergence is measured. M-estimates (e.g., least square estimator) are maximum likelihood-based distances based on the search of the minima of sums of M and S functions. They are the most widely used and are generally considered robust

estimators, but they can give suboptimal results when their assumptions are violated (e.g., errors not-normally distributed). With minimum contrast estimates (e.g., contrast function), *M* and *S* are described as spectral density functions to be minimised. The list and mathematical formulation of the metrics selected in this study is reported in **Table II**. For a more detailed description of the cost function families and of each estimator refer to Leonenko et al. (2013). Gaussian noise ranging from 0 to 10% (with step 1%) was added to the simulated reflectance spectra in order to consider the uncertainties affecting the model and the measured data, and 0 to 20 (with step 1) solutions of the best matching modelled spectra were averaged to mitigate the effect of ill-posedness.

Table II. Selected cost functions (CF) for the description of the distance D[M,S] between measured (M=(m(λ_1), m(λ_2), …, m(λ_n))) and simulated (S=(s(λ_1), s(λ_2), …, s(λ_n))) reflectance spectra. The CFs are grouped in three broad families: information measures, M-estimates and minimum contrast estimates.

CF family	CF	Formula
M-estimates	RMSE	$D[M,S]=\sqrt{\frac{\sum_{\lambda_i=1}^{\lambda_n}(m(\lambda_i)-s(\lambda_i))^2}{n}}$
	Geman-McClure	$D[M,S]=\sum_{\lambda_i=1}^{\lambda_n}\frac{(m(\lambda_i)-s(\lambda_i))^2}{(1+(m(\lambda_i)-s(\lambda_i))^2)}$
Information measures	Kullback-Leibler	$D[M,S]=\sum_{\lambda_i=1}^{\lambda_n} m(\lambda_i)\ln\left(\frac{m(\lambda_i)}{s(\lambda_i)}\right)$
	Jeffreys-Kullback-Leibler	$D[M,S]=\sum_{\lambda_i=1}^{\lambda_n}(m(\lambda_i)-s(\lambda_i))(\ln(m(\lambda_i))-\ln(s(\lambda_i)))$
	Neyman χ-square	$D[M,S]=\sum_{\lambda_i=1}^{\lambda_n}\frac{(m(\lambda_i)-s(\lambda_i))^2}{s(\lambda_i)}$
	K-divergence Lin	$D[M,S]=\sum_{\lambda_i=1}^{\lambda_n} m(\lambda_i)\ln\left(\frac{2m(\lambda_i)}{m(\lambda_i)+s(\lambda_i)}\right)$
	L-divergence Lin	$D[M,S]=\sum_{\lambda_i=1}^{\lambda_n} m(\lambda_i)\ln(m(\lambda_i) + s(\lambda_i)\ln(s(\lambda_i)-(m(\lambda_i)+s(\lambda_i))\ln\left(\frac{m(\lambda_i)+s(\lambda_i)}{2}\right)$
	Harmonique Toussaint	$D[M,S]=\sum_{\lambda_i=1}^{\lambda_n}\left(m(\lambda_i)-\frac{2m(\lambda_i)s(\lambda_i)}{m(\lambda_i)+s(\lambda_i)}\right)$
	Negative exponential disparity	$D[M,S]=\sum_{\lambda_i=1}^{\lambda_n} s(\lambda_i)(\exp\left(-\frac{m(\lambda_i)-s(\lambda_i)}{s(\lambda_i)}\right)-1)$
	Bhattacharyya divergence	$D[M,S]=-\log(1+\sum_{\lambda_i=1}^{\lambda_n}\sqrt{m(\lambda_i)s(\lambda_i)}\ -\frac{1}{2}(m(\lambda_i)+s(\lambda_i)))$
	Shannon	$D[M,S]=-\sum_{\lambda_i=1}^{\lambda_n}\frac{(m(\lambda_i)+s(\lambda_i))}{2}\log\frac{(m(\lambda_i)+s(\lambda_i))}{2} + \frac{1}{2}\left(\sum_{\lambda_i=1}^{\lambda_n} m(\lambda_i)\log(m(\lambda_i))+\sum_{\lambda_i=1}^{\lambda_n} s(\lambda_i)\log(s(\lambda_i))\right)$
Minimum contrast estimation	K(x)=(log(x))²	$D[M,S]=\sum_{\lambda_i=1}^{\lambda_n}(\log(m(\lambda_i))-\log(s(\lambda_i)))^2$
	K(x)=log(x)+1/x	$D[M,S]=\sum_{\lambda_i=1}^{\lambda_n}\left(\log\frac{s(\lambda_i)}{m(\lambda_i)}+\frac{m(\lambda_i)}{s(\lambda_i)}\right)-1$

K(x)=-log(x)+x	$D[M,S]=\sum_{\lambda_i=1}^{\lambda_n}\left(-\log\frac{s(\lambda_i)}{m(\lambda_i)}+\frac{s(\lambda_i)}{m(\lambda_i)}\right)-1$
K(x)=x(log(x))-x	$D[M,S]=1+\sum_{\lambda_i=1}^{\lambda_n}\frac{s(\lambda_i)}{m(\lambda_i)}\left(\log\frac{s(\lambda_i)}{m(\lambda_i)}-1\right)$

The retrieval workflow was performed within ARTMO v. 3.23 (Automated Radiative Transfer Models Operator; http://ipl.uv.es/artmo/) (Verrelst et al. 2011; Rivera et al. 2013), a graphic user interface software package running in MATLAB that includes a suite of leaf and canopy RTMs. ARTMO streamlines the model configuration, running and output storage, thus facilitating the handling and processing of high dimensional spectral data.

The standard fitting statistics such as coefficient of determination (r^2), root mean square error (RMSE), relative RMSE (rRMSE) (i.e., RMSE/mean of measured values), bias (i.e., mean of estimated values – mean of observed values) and relative bias (rbias) (i.e., bias/mean of estimated values) between measured and simulated LCC and LAI were computed to evaluate the performances of the different RTM inversion strategies tested. The leave-one-out cross-validated statistics (r^2_{CV}; $RMSE_{CV}$) were also computed to compare the prediction performance of the different model implementations.

2.4.3 BESS parameterisation strategy and GPP, APAR and LUE estimation

The Breathing Earth System Simulator (BESS) (Ryu et al. 2011; Jiang & Ryu 2016) was used to derive a snapshot of instantaneous GPP over the study area at the time of the *HyPlant* overflight.

BESS is a biophysical model developed to monitor carbon and water fluxes using multi-source remotely sensed data at moderate spatial resolution (1-5 km). The model couples a 1-dimensional atmospheric radiative transfer module to compute direct and diffuse radiation in the PAR and NIR spectral regions (Kobayashi & Iwabuchi 2008; Ryu et al. 2018), a two-leaf and two-stream canopy radiative transfer model to compute the absorbed PAR and NIR radiation by sunlit and shaded leaves respectively (de Pury & Farquhar 1997; Ryu et al. 2011), and an integrated carbon assimilation-stomatal conductance-energy balance model (Ball et al. 1988; Paw & Gao 1988) to compute GPP and ET. In its original configuration, BESS uses as input MODIS atmosphere (e.g., cloud optical thickness, aerosol optical thickness, water vapour, ozone) and land products (e.g., LAI, land cover, albedo in PAR and NIR spectral regions) as well as other satellite data (e.g.,

OCO-2-NOAA data to derive CO_2 concentration maps; Shuttle Radar Topography Mission (SRTM) data to take into account the effect of altitude on incoming radiation).

For this study, BESS was customised to ingest *HyPlant* high-resolution (1 m) products and atmospheric constraints obtained from meteorological data collected in the field, outputting a BESS-GPP map at the time of *HyPlant*'s overflight at high spatial resolution.

Four *HyPlant*-derived spatially resolved products were used to feed BESS: two broadband reflectance maps and two key plant trait maps. Broadband reflectance was calculated from the DUAL hyperspectral reflectance cube with a weighted average after a regular spectral resampling (1 nm spectral interval) in the VIS (400-700 nm) and NIR (841-876 nm) spectral regions, respectively. Maximum carboxylation rate normalised to 25°C ($Vcmax_{25}$) and LAI were derived from the RTM inversion. While LAI is a direct output of the RTM, $Vcmax_{25}$ was empirically inferred from LCC using a linear relationship for broadleaved forest species found by Croft et al. (2017). This study found a strong linear relationship (r^2=0.78, $p<0.001$) between the two variables across three growing seasons considering four different deciduous tree species, demonstrating that LCC can be a reliable proxy for modelling Vcmax. $Vcmax_{25}$ map was then derived from the LCC map obtained as output of the RTM inversion according to **Eq. 1** (Croft et al. 2017):

$$Vcmax_{25} = 1.3 \times LCC + 3.72 \quad \textbf{Eq. 1}$$

Additionally, atmospheric forcings such as air temperature, pressure, column water vapour, relative humidity and aerosol optical thickness were obtained from punctual measurements acquired with a Microtops II sunphotometer (Solar Light Company, Glenside, USA). The incident solar irradiance during the overpass was collected in the spectral region 350-2500 nm with a calibrated FieldSpec 4 (ASD Inc., Longmont, USA) measuring over a levelled white Spectralon (Labsphere, North Sutton, USA).

2.5 *HyPlant* data product comparison

The outputs obtained from *HyPlant* DUAL and FLUO images (e.g., F_{687}, F_{760}, GPP) were inter-compared by fitting regression models between pairs of variables. The statistical analysis was performed in R testing different models to find the best fit. One underlying assumption when using linear or nonlinear models is the independency of observations. This is not met in case of spatial-autocorrelation in the data, meaning that

clusters of data points present numerical similarity because of their spatial proximity (Haining 1980). The spatial dependency implicates that part of the information within the dataset is repeated and therefore redundant. In order to detect a possible violation of the independency assumption, an analysis of the semivariograms of the images was performed. Based on the results of this analysis, all the airborne-derived products were aggregated at tree crown level (i.e., all the pixels belonging to the same tree crown were averaged) for spatial comparison instead of performing a pixel by pixel comparison. Beyond bypassing the issues related to the spatial dependency, this approach allowed reducing noise in the data and mitigating the slight geometric mismatch between the images recorded from *HyPlant* DUAL and FLUO modules.

3 Results

3.1 *HyPlant* data products

3.1.1 Red & far-red sun-induced chlorophyll fluorescence maps

The high-spatial resolution F_{687} and F_{760} maps obtained over the forest using the SFM implemented for the processing of *HyPlant* imagery are shown in **Fig. 2**.

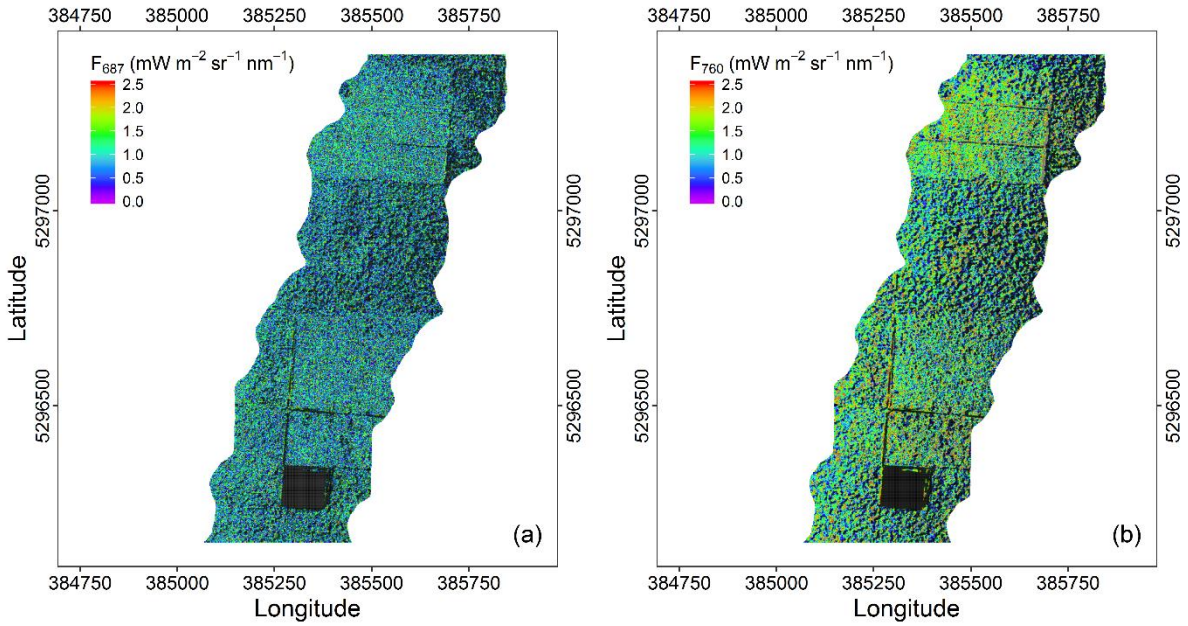

Figure 2. F_{687} (a) and F_{760} (b) maps obtained from *HyPlant* hyperspectral radiance using the spectral fitting method.

Overall, the magnitude of F_{760} ranged from 0 to 2.5 mW m^{-2} sr^{-1} nm^{-1}, with a frequency peak around 1.5 mW m^{-2} sr^{-1} nm^{-1}, while F_{687} ranged from 0 to 2 mW m^{-2} sr^{-1} nm^{-1}, with values around 0.8 mW m^{-2} sr^{-1} nm^{-1} occurring more frequently. These values were consistent throughout the image and coherent with the ones usually observed on forested areas by ground-based measurements. The spatial patterns were meaningful for both F_{687} and F_{760}: higher fluorescence was observed in correspondence of the sunlit part of the canopy, lower fluorescence was observed in the inter-crown gaps and non-fluorescing targets such as bare soil and asphalt exhibited values close to zero. On the other hand, F_{687} was characterised by a higher noise in the retrieval which resulted into a remarkable 'salt-and-pepper' effect on the map. A quantitative evaluation of the SFM performance in estimating F was carried out comparing the airborne with the ground-based retrievals measured in correspondence of six selected targets (**Fig. 3**).

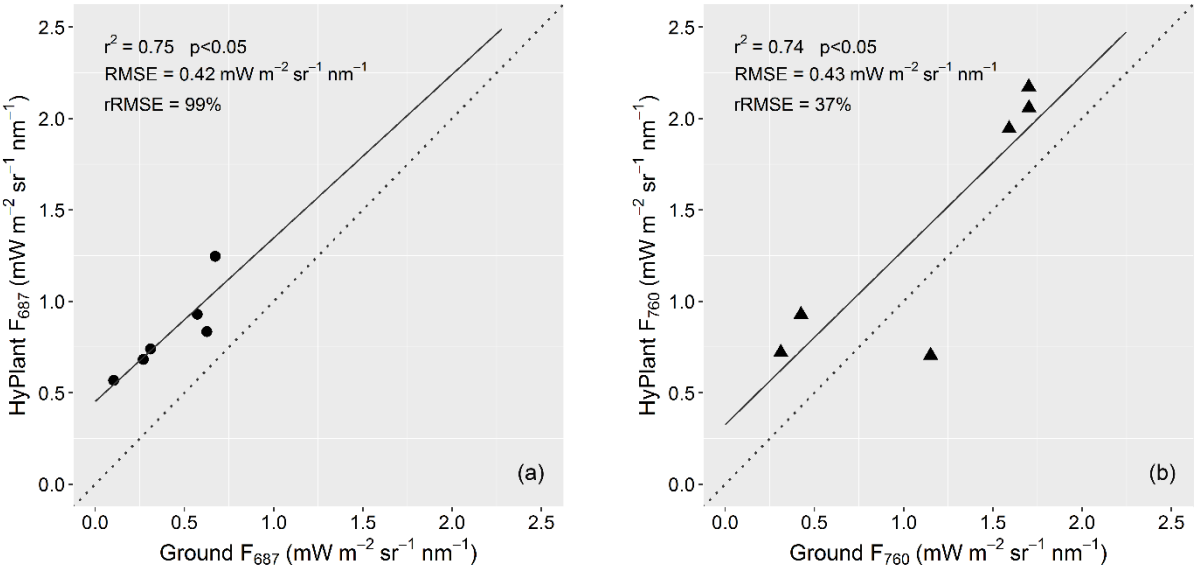

Figure 3. Comparison between ground-based and airborne F_{687} (a) and F_{760} (b) retrievals in correspondence of different forest species. The solid line corresponds to the linear model fitted between the paired variables. The dotted line represents the 1:1 line.

The comparison showed consistency between airborne and ground F measured both in the red and far-red regions of the spectrum for different canopies. The linear models fitted between airborne and ground-based observations were statistically significant ($p<0.05$) and showed the effectiveness of the SFM in F_{687} (r^2=0.75; RMSE=0.42 mW m^{-2} sr^{-1} nm^{-1}) and F_{760} (r^2=0.74; RMSE=0.43 mW m^{-2} sr^{-1} nm^{-1}) retrieval. In terms of

absolute values, a systematic overestimation of F_{687} measured from *HyPlant* compared to the ground references was noticed (bias=0.41 mW m^{-2} sr^{-1} nm^{-1}; rbias=52%). This effect was smaller in F_{760} retrieval (bias=0.27 mW m^{-2} sr^{-1} nm^{-1}; rbias=17%).

3.1.2 Plant trait maps

The results of the GSA performed on the coupled PROSPECT-4-INFORM model are shown in **Fig. 4**. For each input parameter of the RTM, the total-order sensitivity index obtained (SI) is expressed in percentage as a function of the wavelength. The analysis revealed a small influence of the leaf structural parameter, tree height and average leaf inclination across all the spectrum. These parameters were therefore set to constant values in order to allow maximising the variability of the other input variables.

The LCC and LAI maps at high spatial resolution obtained as output of the RTM-based retrieval from *HyPlant* DUAL imagery are shown in **Fig. 5**.

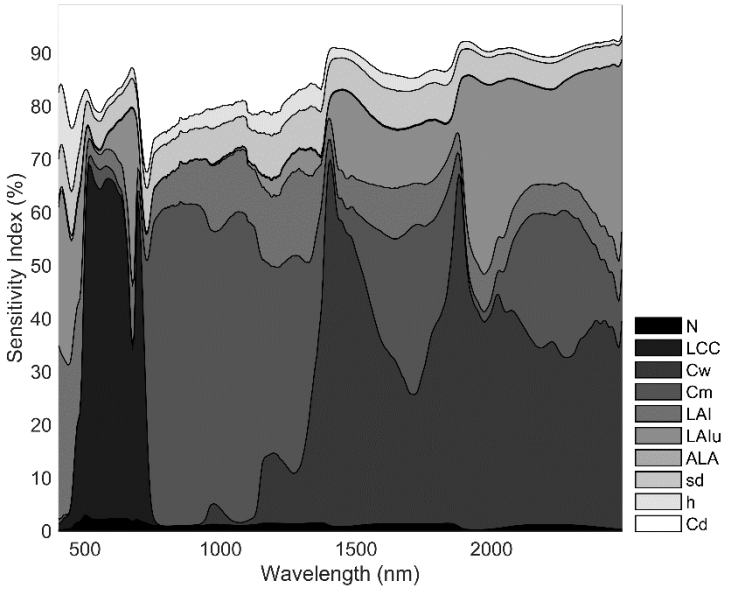

Figure 4. Results of the GSA of the coupled PROSPECT-4-INFORM RTM. The total-order sensitivity index (SI) is expressed in % for each input parameter as a function of the wavelength. The acronyms in the legend correspond to leaf structural parameter (N), leaf chlorophyll content (LCC), leaf water content (Cw), leaf dry matter content (Cm), leaf area index (LAI), leaf area index of the understory (LAIu), average leaf inclination (ALA), stem density (sd), tree height (h) and crown diameter (Cd).

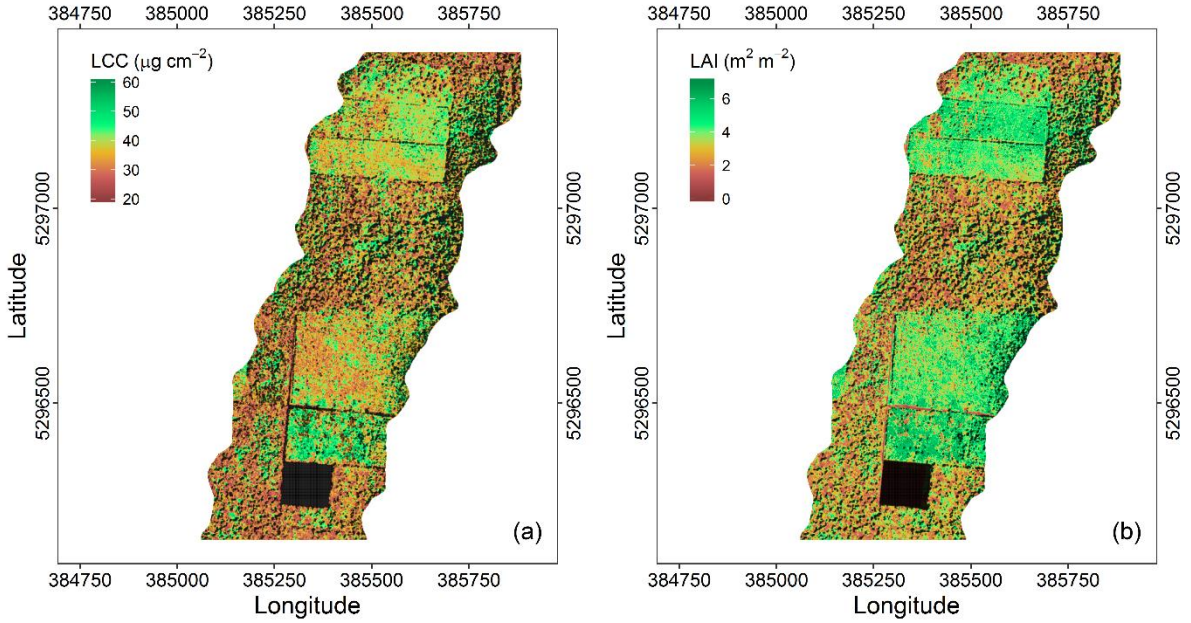

Figure 5. LCC (a) and LAI (b) high-resolution maps obtained from *HyPlant* DUAL data through LUT-based inversion of the coupled PROSPECT-4-INFORM RTM using the optimal inversion strategy.

Strong correlations were found between measured and predicted values of LCC and LAI, demonstrating that the inversion of the INFORM model constrained with various regularisation techniques yields accurate retrievals of plant traits in forest ecosystems.

LCC was most accurately retrieved using a logarithmic minimum contrast cost function based on the minimisation of the distance (contrast) between a parametric model and a non-parametric spectral density (Leonenko et al. 2013). The best fitting (r^2=0.65, $p<0.001$; n=21) was obtained using the mean of the ten best solutions and no addition of random noise to the simulations. The use of a divergence measure cost function formalised by Kullback and Leibler (1951), based on the minimisation of the distance between two probability distributions, showed the best performances in the retrieval of LAI. As for the retrieval of LCC, the best results were obtained using ten best solutions and no addition of random noise (r^2=0.72, $p<0.001$; n=14). The summary statistics in fitting and cross-validation of the linear regressions between measured and estimated LCC and LAI are reported in **Table III**. The scatterplots showing the measured LCC and LAI values against the predicted ones are reported in **Fig. 6**.

Table III. Summary of statistics in fitting (r^2, RMSE, rRMSE, bias, rbias) and cross-validation (r^2_{CV}, $RMSE_{CV}$) of the comparison between measured and estimated LCC and LAI values.

Plant trait	r^2	r^2_{CV}	RMSE	$RMSE_{CV}$	rRMSE	bias	rbias
LCC	0.65	0.58	5.66 (μg cm^{-2})	3.96 (μg cm^{-2})	15 (%)	2.61 (μg cm^{-2})	7 (%)
LAI	0.72	0.47	0.51 (m^2 m^{-2})	0.57 (m^2 m^{-2})	14 (%)	0.04 (m^2 m^{-2})	1 (%)

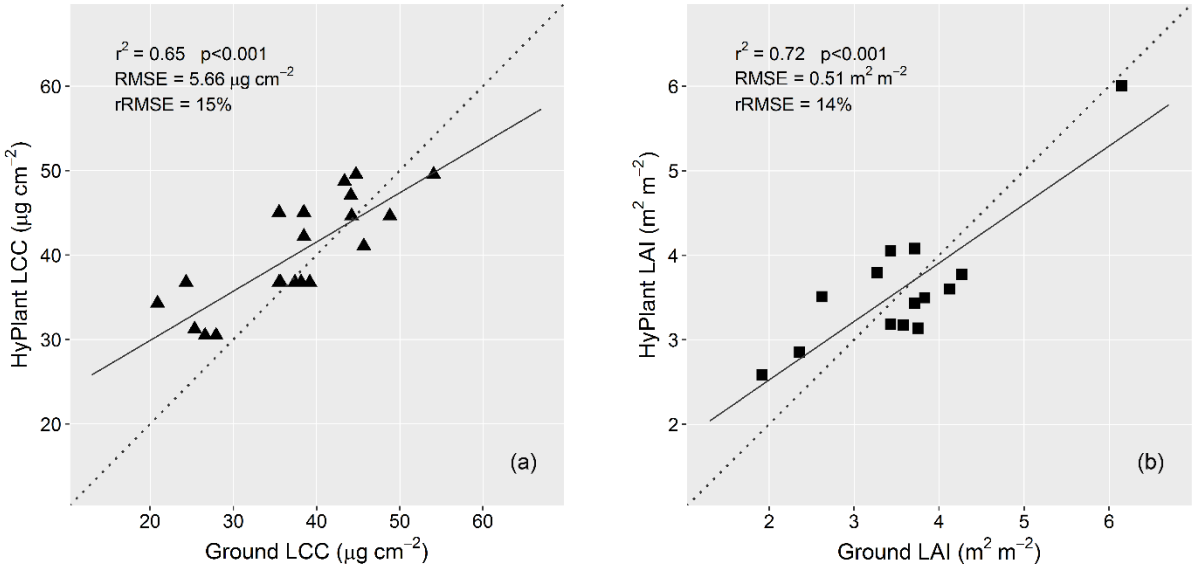

Figure 6. Comparison between ground-based measurements and *HyPlant* estimates of LCC (a) and LAI (b). The solid line corresponds to the linear model fitted between the paired variables. The dotted line represents the 1:1 line.

Overall, LCC and LAI showed reasonable value distributions and meaningful spatial patterns within the complex mixed forest ecosystem. The LCC and LAI maps showed some similarities, but they were not totally correlated (r^2=0.5, p<0.001). Based on the species distribution in the study area obtained from the classification performed in Tagliabue et al. (2016) using APEX airborne data, it was observed that field maple and small-leaved linden were the species characterised by the highest LCC values, even though the differences compared to the other species were not remarkable. LAI showed a larger inter-species variability, with the highest value for small-leaved linden and the lowest for Scots pine. In general, LCC did not differ significantly in regeneration and mature stands, while LAI was higher in regeneration stands.

3.1.3 GPP, APAR and LUE maps

The incorporation of spatialised maps of key plant traits into the process-based BESS model allowed obtaining spatial maps of GPP, APAR and LUE at high spatial resolution (**Fig. 7**).

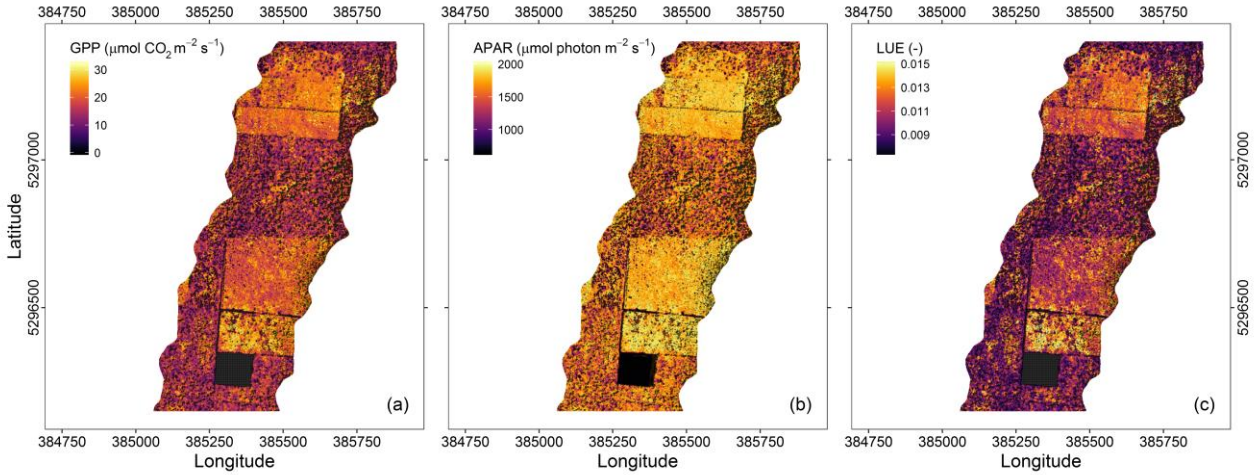

435

436 **Figure 7. GPP (a), APAR (b) and LUE (c) maps obtained from the BESS model driven with airborne-**
437 **derived high-resolution maps.**

438 The map of instantaneous GPP showed values ranging from 0 µmol CO_2 m^{-2} s^{-1} for bare soil up to ~30
439 µmol CO_2 m^{-2} s^{-1} for dense vegetation. The regeneration areas, where trees were planted with higher density
440 and both LCC and LAI were higher, were clearly distinguishable in the image due to their larger CO_2
441 assimilation. In the mature stands, the crown-shadow patterns were more evident and the GPP values were
442 generally lower, even though with an appreciable variability across the image. It is worth noting that, due to
443 the nature of the model and the available input data, the obtained modelled GPP was considerably driven by
444 LAI and $Vcmax_{25}$ (r^2=0.94 and r^2=0.68 respectively, p<0.001). However, LAI and $Vcmax_{25}$ were only weakly
445 related (r^2=0.5, p<0.001).

446 APAR varied from 0 to ~1900 µmol photon m^{-2} s^{-1} and the patterns in the map resembled the ones
447 observed in GPP (r^2=0.82, p<0.001), despite a lower variability for high APAR values. LUE, obtained as ratio
448 between modelled GPP and APAR, ranged from 0 to 0.018 and appeared strongly related to both the GPP
449 (r^2=0.76, p<0.001) and APAR maps (r^2=0.8, p<0.001).

450 **3.2 Linking measured F and modelled BESS-GPP, -APAR and -LUE**

451 The analysis of the semivariograms of the images obtained from *HyPlant* revealed the presence of a clear
452 spatial autocorrelation in the data. This effect exists within a range from 0 to 10-15 m, as it can be gathered
453 from the range (i.e., the distance expressed in meters at which the semivariogram levels) of the

semivariogram function showed in **Fig. 8**. This distance corresponds to the average diameter of the tree crowns, indicating that there is a high similarity among pixels of the same crown. For this reason, the spatial relationships between the airborne-derived outputs showed hereafter are referred to the data aggregated at tree crown level.

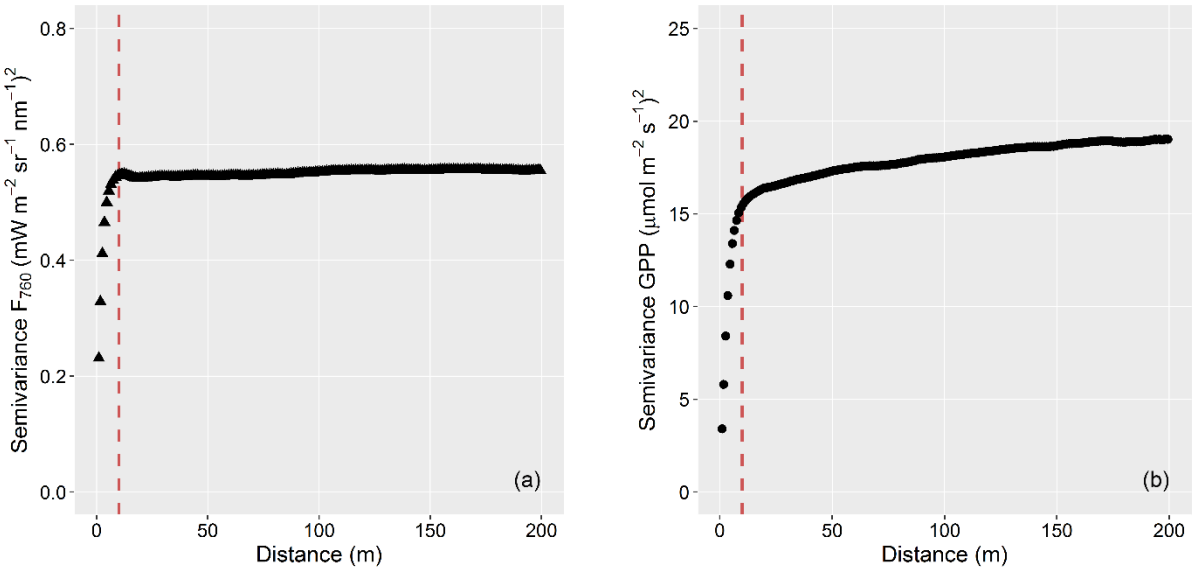

Figure 8. Semivariogram functions of the F_{760} (a) and GPP (b) images expressed as a function of the distance (m). The red dashed lines represent the range of the semivariogram functions.

The spatial relationships between F_{687} and F_{760} retrieved from *HyPlant* ultra-fine spectral resolution radiance data and GPP, APAR and LUE obtained as outputs of the BESS model driven with airborne-derived data are shown in **Fig. 9**. In the scatterplots, each data point is the average of all the sunlit pixels of the same tree crown.

Different regression models were tested between the paired variables. Overall, we found that the relationships were best fitted by a logarithmic model, that allowed describing the nonlinearity of the relationships. A positive logarithmic relationship was found between F_{760} and GPP (r^2=0.46, $p<0.001$), F_{760} and APAR (r^2=0.43, $p<0.001$) and between F_{760} and $Vcmax_{25}$ (r^2=0.17, $p<0.001$). Conversely, no significant relationship was found between F_{687} and GPP, F_{687} and APAR or F_{687} and $Vcmax_{25}$ ($p>0.05$). In order to remove the influence of APAR, the relationships between the F yields and LUE were analysed. The results showed an opposite behaviour of the red (Fy_{687}) and far-red (Fy_{760}) F yields: Fy_{760} showed a positive

logarithmic relationship with LUE (r^2=0.19, p<0.001), while Fy_{687} and LUE were found to be negatively correlated (r^2=0.25, p<0.001) (**Fig. 9 d, h**).

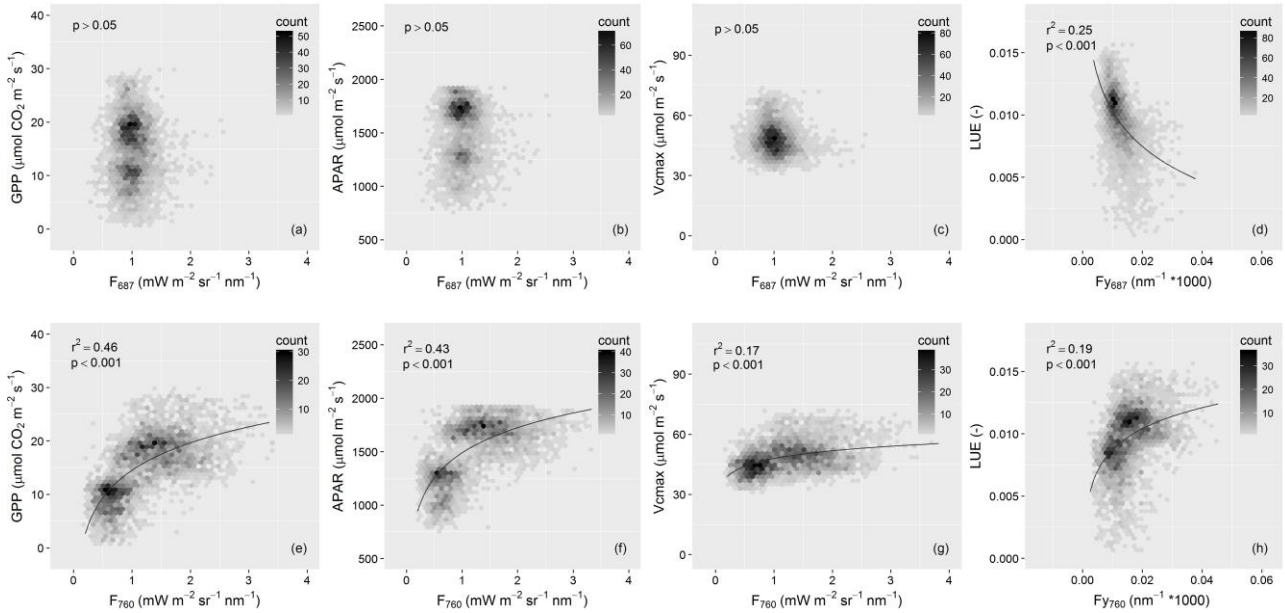

Fig. 9. Relationships at tree crown level between: (a) F_{687} and GPP, (b) F_{687} and APAR, (c) F_{687} and $Vcmax_{25}$, (d) Fy_{687} and LUE, (e) F_{760} and GPP, (f) F_{760} and APAR, (g) F_{760} and Vcmax and (h) Fy_{760} and LUE. The colour scale represents the point density. The solid curves correspond to a logarithmic model fitted between the paired variables.

4. Discussion

The quantitative estimation of vegetation traits is required in a variety of ecological applications. Regardless the considerable advances achieved through the development and testing of a wide range of leaf as well as canopy-level retrieval methods (Verrelst et al. 2015a), their quantification from remotely sensed data remains challenging. The inference of these traits is in fact concealed by confounding factors related to the canopy (e.g., canopy structure, background influence, illumination effects), the atmosphere (Malenovský et al. 2013; Houborg et al. 2015b) and the sun-sensors geometries, that might introduce large inaccuracies in the retrieved traits. The inversion of physically based RTMs is generally recognised as a reliable and accurate approach (Atzberger et al. 2015; Dorigo et al. 2007). However, the use of regularisation strategies is critical to

mitigate the drawbacks of ill-posedness and to obtain trustworthy results (Verrelst et al. 2014; Combal et al. 2003). In this study, LCC was accurately estimated with an r^2 of 0.65 and RMSE of 5.66 μg cm^{-2} (refer to **Table 3** for the complete summary of statistics) by inverting the canopy-level INFORM model coupled with the leaf-level PROSPECT-4 model. Previous studies conducted in similar contexts showed estimation accuracies ranging from ~4.5 to ~13.5 μg cm^{-2} depending on the inversion strategy, sensor configuration and study site characteristics. Croft et al. (2013) obtained an accuracy of 6.42 μg cm^{-2} (r^2=0.62) inverting the PROSPECT-4Scale model (Chen & Leblanc 1997) in a mixed forest site using MERIS satellite data, that degraded to 10.45 μg cm^{-2} (r^2=0.41) when inverting the model on CASI airborne spectral data. Croft et al. (2015) further achieved an accuracy of 7.05-13.40 μg cm^{-2} (r^2=0.79-0.38) using the same model in a follow-up study. Inverting the PROSPECT-DART model (Gastellu-Etchegorry et al. 1996) in coniferous sites, Hernandez-Clemente et al. (2014) and Malenovský et al. (2013) obtained LCC estimates with an RMSE of 5.03 μg cm^{-2} (r^2=0.54) and of 2.27-12.30 μg cm^{-2} (r^2=0.72-0.41), respectively. It is worth noting that none of the aforementioned studies tested the use of regularisation options to constrain the model inversion apart from the use of prior information to restrict the variability of the model input parameters. In this study, LAI was estimated using the same LUT-parameterisation as for LCC of the coupled PROSPECT-4-INFORM model, obtaining an r^2 of 0.72 and RMSE of 0.5 m^2 m^{-2} (refer to **Table 3** for the complete summary of statistics) compared to the ground measurements. Similar results were obtained inverting the INFORM model in broadleaved as well as coniferous forests by Wang et al. (2018) (RMSE=0.43 m^2 m^{-2}; r^2=0.63), Yang et al. (2011) (RMSE=0.41 m^2 m^{-2}; r^2=0.74), Atzberger et al. (2000) (r^2=0.57) and Schlerf & Atzberger (2006) (RMSE=0.58 m^2 m^{-2}; r^2=0.73). The latter authors achieved lower accuracies (RMSE=0.74-0.94 m^2 m^{-2}; r^2=0.51-0.57) using the same model applied on multi-directional CHRIS-PROBA satellite data (Schlerf & Atzberger 2012). Similar results were achieved using different RTMs, e.g. Omari et al. (2013) inverted the PROFLAIR model (White et al. 2001) in a broadleaf-dominated forest obtaining an estimation accuracy of 0.47 m^2 m^{-2} (r^2=0.59) and Banskota et al. (2015) used DART to estimate LAI in a deciduous forest with an accuracy of 0.5-0.74 m^2 m^{-2} (r^2=0.6-0.64). Overall, the LAI estimation accuracy reported in literature ranges between ~0.4 and ~0.9 m^2 m^{-2}. A systematic assessment of using different strategies for minimising the ill-posedness of the inversion has

514 not been performed in studies conducted in forest ecosystems yet. However, it can be grasped from the
515 previous works that the use of even few regularisation options (e.g., prior information about the input
516 parameters, multiple best solutions of the inversion, ecological rules to exclude unrealistic solutions) usually
517 leads to more accurate LAI retrievals. In this study, the coupled PROSPECT-4-INFORM model was
518 successfully inverted providing reliable LCC and LAI spatialised maps in a mixed forest site. Besides the
519 representativeness of the model, which provides a fair compromise between realism and simplicity, the
520 parameterisation of the model to generate the LUT and the recourse to regularisation options were found to
521 be advisable to obtain accurate retrievals, as highlighted in analogous studies conducted on crops (Verrelst
522 et al. 2015b). The prior knowledge about the variability of the model input parameters allowed excluding
523 unlikely combinations that constitute a source of error and unnecessarily increase the LUT size. Likewise,
524 the global sensitivity analysis allowed an optimised model parameterisation: redundant information in the
525 LUT due to multiple combinations carrying the same information was avoided, while the variability of most
526 sensitive model parameters was maximised.

527 Consistently with the findings of Wang et al. (2018), who performed a sensitivity analysis of the
528 PROSPECT-5-INFORM model, the leaf water content and leaf dry matter content showed a great influence
529 on the modelled canopy reflectance (**Fig. 4**). In addition, a great contribution of LCC to the variation of
530 canopy reflectance was observed in the visible part of the spectrum, which was not considered in Wang et al.
531 (2018). At the canopy level, the most affecting variables across the spectrum were LAI (understory and
532 overstory) and crown diameter, while the stem density had a moderate influence on the output. This is not
533 in complete agreement with the aforementioned study, but the authors suggested a mutual compensation
534 between the three canopy structural parameters. Since the stem density did not vary much in our study site,
535 it is likely that this resulted into a larger influence of LAI. Leaf structural parameters, canopy height and
536 average leaf inclination, which showed a negligible effect on the reflectance variation, were fixed to
537 maximise the predictive power of the model. Regarding the LUT-based inversion strategy, various
538 optimisation options were tested in this work, including the use of different cost functions to match
539 measured and modelled spectra, the addition of gaussian noise to the simulated data and the use of multiple

solutions of the inversion. Our results showed a considerable impact of the choice of the cost function used to minimise the distance between the measured and simulated spectra on the retrieval of both LCC and LAI. As observed by Verrelst et al. (2014) in a study focused on the LUT-based retrieval of LCC and LAI in crops, we found that the use of the classical RMSE always led to sub-optimal results. The use of multiple best solutions also improved the estimates, although not being as impacting as the choice of the cost function. The addition of random noise to the simulations did not affect the retrieval in our case.

Beyond focusing on the retrieval of reflectance-based products, this work aimed at analysing the spatial variability of red and far-red sun-induced chlorophyll fluorescence across the study site, which constitutes a more direct proxy of the vegetation functional state (Wieneke et al. 2016). F_{687} and F_{760} were estimated using the spectral fitting methods with an r^2 of 0.75 and 0.74 ($p<0.05$), respectively, as assessed from the comparison against the ground-based measurements. The SFM was exploited for the first time in this study to map the distribution of F at both the emission peaks over a forest area. F quantification using the SFM offers several advantages compared to other retrieval methods, e.g., the exploitation of the oxygen absorption bands, where the signal is proportionally way larger than in the solar Fraunhofer lines, and the physical nature that makes it independent from the observed scene. On the other hand, the SFM approach requires a rigorous atmospheric correction scheme, which is not needed when using other methods exploiting the dark lines in the solar spectrum (e.g., Guanter et al. 2012; Damm et al. 2014).

The known challenges posed by the retrieval of red F (e.g., the narrower shape of the O_2-B band compared to O_2-A and the overall lower signal detectable from above due to the reabsorption within the leaf and the canopy) resulted into a higher uncertainty in the retrieval of F_{687}, which appeared noisier than F_{760} at full resolution (1 m). However, the aggregation of the data at crown level for further analysis reduced this issue in consequence of noise averaging.

Recently, F has been exploited to study photosynthetic activity of vegetation from RS. This is based on the mechanistic link that exists between F emission, photochemistry and heat dissipation. However, this relationship is multifaceted and multiple gaps still need to be filled to have an unbiased understanding of the link between F and apparent photosynthesis (i.e., GPP). In particular, it remains unclear how far-red F

566 and GPP are related at high spatial resolution and how red F is related to GPP. To address these questions,
567 we used the BESS model to derive GPP, APAR and LUE over the study site and to get insights into the
568 relationships existing between red, far-red F and these variables at tree crown level.

569 The high-resolution GPP, APAR and LUE maps obtained driving the model with airborne-derived
570 inputs, taking into account inevitable model simplifications, are representative of the instantaneous carbon
571 uptake, light absorption and light use efficiency at the time of *HyPlant*'s overpass. BESS is a process-based
572 model, and its performances in predicting GPP were comprehensively evaluated in Ryu et al. (2011), Jiang &
573 Ryu (2016) and Whitley et al. (2016). Ryu et al. (2011) validated the model at the global scale against eddy
574 covariance tower flux data from 33 FLUXNET sites covering a broad range of plant functional types. The
575 strong linear relationship found with modelled GPP (r^2=0.86, relative bias: 5%) at annual composite provided
576 experimental evidence of the model capacity to produce accurate GPP estimates. Further evaluation of the
577 model was carried out in Jiang & Ryu (2016) by means of a comparison against a set of 113 FLUXNET sites
578 distributed worldwide in the period 2000-2015. The results at both 8-daily and annual composites confirmed
579 the reliability of the model in predicting GPP (r^2=0.67 and r^2=0.93, respectively, compared to flux
580 measurements). In Whitley et al. (2016), BESS was benchmarked against a set of models of increasing
581 complexity, showing consistent performances with other terrestrial biosphere models. With respect to the
582 ordinary BESS implementation, the differences in our study mainly reside in the high-spatial resolution data
583 used to feed the model and in the snapshot nature of the analysis. The unavailability of eddy covariance
584 tower data in the study site limited our possibility to directly compare *HyPlant*-BESS outputs with ground-
585 based flux estimates, anyhow, a proper validation would have been critical even in case of their availability.
586 The flux tower information is in fact a point measurement, which is valuable for monitoring the temporal
587 variation of the carbon fluxes but is difficult to exploit for assessing their spatial variability. Because of the
588 high-detail nature of this snapshot analysis and of the data available, a more likely option to check the model
589 performances was the comparison between modelled variables and proxies of these variables that can be
590 remotely sensed. As shown in **Fig. 10**, BESS-fAPAR (i.e., fraction of APAR, calculated as ratio between BESS-
591 APAR and incoming PAR) was found to be highly correlated to VIs which are well-known to be related to

the fraction of absorbed PAR. BESS-fAPAR showed the strongest correlation with VIs such as NDVI (Rouse et al. 1974) (r^2=0.86, p<0.001) and NDVIre (Gitelson & Merzlyak 1994) (r^2=0.86, p<0.001), which are sensitive to the photosynthetic component of the canopy. Conversely, the correlation with VIs related to the totality of the canopy such as NDSI (Inoue et al. 2008) was found to be lower (r^2=0.63, p<0.001). This further supports the correct representation of the carbon fluxes by the model, since the modelled APAR that is used to estimate GPP is representative of canopy component which is effectively involved in photosynthesis.

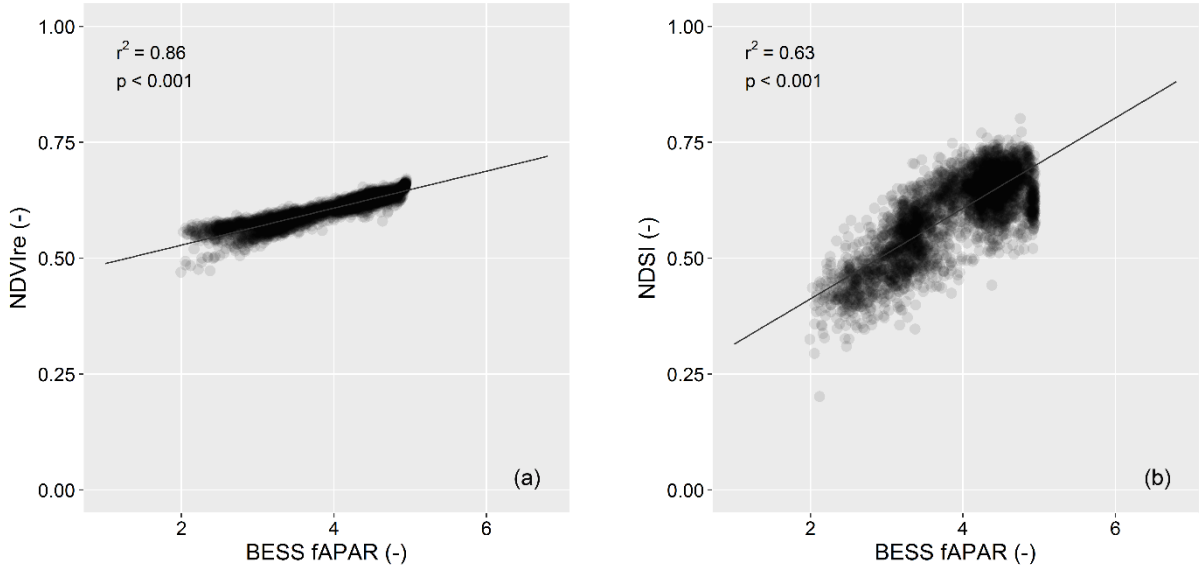

Fig. 10. Relationships at tree crown level between BESS derived fAPAR and VIs: BESS-fAPAR and NDVIre (a); BESS-fAPAR and NDSI (b).

The soundness of *HyPlant*-BESS results was made possible by the accurate spatial representation of LAI and LCC (from which $Vcmax_{25}$ was empirically derived) obtained through RTM inversion. These two variables constitute the two main drivers of BESS according to the sensitivity analysis performed in Ryu et al. (2011). Some potential uncertainties in GPP modelling can be associated with the use of LCC to infer $Vcmax_{25}$.

The relationship between far-red F and GPP has been shown to be strong in several studies conducted at different spatio-temporal scales over different vegetation types. Multiple studies exploiting satellite data showed a linear relationship between global scale annual averages of spaceborne F retrievals and data-driven upscalings of GPP from EC tower measurements (Frankenberg et al. 2011; Joiner et al. 2011; Guanter

et al. 2014). However, different results were obtained in studies conducted at local and regional scales as well as modelled data. Several authors found nonlinear and ecosystem-specific relationships (e.g., Damm et al. 2015; Zhang et al. 2016; Goulas et al. 2017), revealing that this link is more complex at finer spatial resolution. As a matter of fact, this relation is the reflection of a complex interplay between species-specific functional traits and of the different functional strategies used to balance the photochemical and non-photochemical light dissipation (van der Tol et al. 2014). In addition, the distribution of the absorbing and scattering elements within the canopy determines the canopies to act as photon traps (Lewis & Disney 2007; Knyazikhin et al. 2013). As a consequence, the escape probability of photons is a function of the complexity of the canopy architecture. All these factors modulate the F signal detected by the sensor, that in turn might be nonlinearly correlated with GPP when the scale of observation allows appreciating these effects.

Working at individual tree crown scale, we found a statistically significant positive nonlinear relationship between measured F_{760} and modelled GPP (r^2=0.46, $p<0.001$), confirming the previous findings and demonstrating that even in a snapshot case an empirical relationship between the spatial variation of the two variables exists. However, the pronounced scattering of the data points suggests that there are other factors affecting the relationship that are apparently masked when working at broader spatial and/or temporal scales. To understand whether this actually depends on the scale of observation, the effect of spatial degradation was tested on our data by aggregating *HyPlant* high resolution images at increasing spatial resolutions (i.e., 10 m-20 m-40 m-80 m) (**Fig. 11**). In contrast with the results showed in **Fig. 9**, where the data were aggregated at crown level, the spatial aggregation exercise showed in **Fig. 11** provides an insight on situations that could be potentially observed at satellite scale, where the coarser spatial resolution does not allow working at individual crown level anymore.

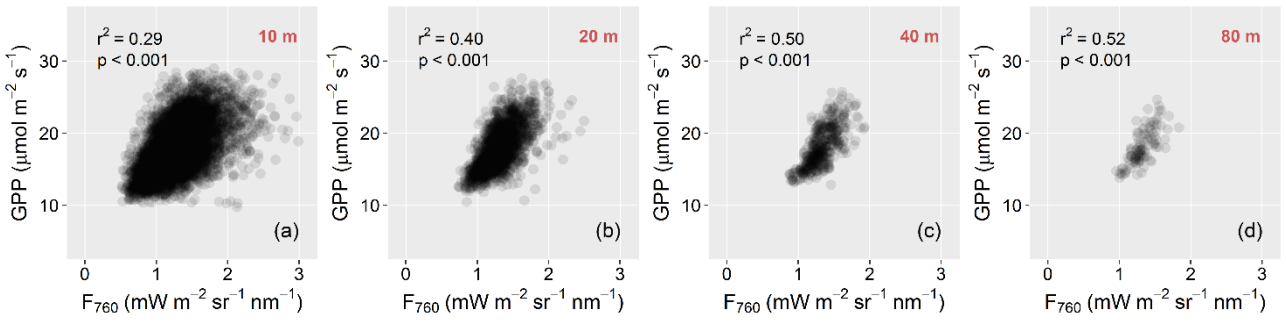

Fig. 11. Relationship between F_{760} and BESS-GPP at increasing spatial aggregation: (a) 10 m, (b) 20 m, (c) 40 m and (d) 80 m.

The clear progressive decrease of the scattering along with the increase of the correlation (i.e., r^2=0.29 at 10 m resolution and r^2=0.52 at 80 m resolution) suggests that the averaging of the spatial heterogeneity effectively improves the relationship between F and GPP. It can be also noticed that the relationship tends to become more linear as the spatial resolution increases, which is somewhat similar to what Zhang et al. (2016) and Damm et al. (2015) observed in the temporal dimension and might be explained by the reduction of the variability across the study site and by the changing impact of the confounding effects of canopy structure at coarser spatial resolution. A similar correlation was observed between F_{760} and APAR (r^2=0.43, $p<0.001$). APAR has been shown to be the main driver of F_{760} temporal variability because of its large variation (Miao et al. 2018; Yang et al. 2015; Li et al. 2018; Koffi et al. 2015; Rossini et al. 2010, Yang et al. 2018). To disentangle such influence of APAR in the relation between F_{760} and GPP, the relationship between Fy_{760} (F_{760}/APAR) and LUE (GPP/APAR) was examined, revealing a significant positive nonlinear correlation (r^2=0.19, $p<0.001$) between the two variables. This result is consistent with the findings of Yang et al. (2015), Zhang et al. (2016) and Verma et al. (2017), supporting the hypothesis that F_{760} contains information not only on APAR, but on both the terms that constitutes the equation GPP = APAR × LUE. Other studies conducted in the temporal domain found an opposite behaviour. For example, a recent work conducted by Yang et al. (2018) in a rice paddy site found that far-red F is a better proxy of APAR than GPP at high temporal resolution, suggesting a different meaning of the relationship between F, GPP and APAR in the spatial and temporal domain. Regarding F emitted in the red region, some studies suggested that it might be a more sensitive indicator of plants' photosynthetic activity due to the greater contribution of photosystem II in this region (Verrelst et al. 2015d; Baker et al. 2008; Porcar-Castell et al. 2014). Following this hypothesis, simulation studies conducted using the SCOPE model (van der Tol et al. 2009) showed that the relationship between red F and GPP should be similar or even better than the one observed between far-red F and GPP (Zhang et al. 2016; Verrelst et al. 2016). However, the few studies that exploited real red F observations to validate this finding showed contradictory results. While in Cheng et al. (2013) red F performed better than far-red F in predicting GPP,

Goulas et al. (2017) and Liu et al. (2017) concluded that far-red F is a better proxy of GPP, especially when considering canopies with varying biochemical and structural composition. This is supported by the modelling results of Du et al. (2017) and Liu et al. (2018), that show a heavily scattered relationship between red F and APAR compared to the one between far-red F and APAR, because of the greater influence of LCC and LAI variation. In our study, no significant correlation was found between the spatial variability of F_{687} and GPP and APAR. Yet, interestingly a statistically significant negative correlation emerged when normalising both red F and GPP by APAR (r^2=0.25, $p<0.001$). To the best of our knowledge, whilst both positive and negative correlations were shown to be possible between Fy_{760} and LUE depending on the energy partitioning (Miao et al. 2018), no previous study investigated the relationship between Fy_{687} and LUE. Hence, further studies need to be performed in order to be able to interpret this finding. A possible explanation could be related to the role of reabsorption within the canopy, which has a strong effect on red F while almost not affecting far-red F.

5. Conclusions

In this study, *HyPlant* airborne high-resolution images acquired over a mixed forest ecosystem were exploited to obtain and analyse the spatial intra- and inter-variability of different variables related to vegetation biochemical, structural and functional state. Firstly, LCC and LAI, two key variables in vegetation-related studies, were estimated with accuracy of 5.66 μg cm^{-2} and 0.51 m^2 m^{-2}, respectively, by inverting the coupled PROSPECT-4-INFORM radiative transfer model. The high accuracy of the two spatialised products as well as their consistent spatial patterns were made possible by an optimal parameterization and inversion strategy applied on *HyPlant* hyperspectral data. Secondly, high-resolution maps of sun-induced chlorophyll fluorescence, an indicator of plants' photosynthetic activity, were obtained for the first time at both the red and far-red peaks over a forested area. The comparison against top-of-canopy measurements acquired at the same time of the overpass highlighted the accuracy of the estimates, demonstrating the reliability of the SFM retrievals (r^2=0.73 at O_2-B band; r^2=0.74 at O_2-A). Third, the spatialised plant traits obtained through RTM inversion were successfully exploited to drive a customised version of the Breathing Earth System Simulator (BESS), which provided GPP, APAR and LUE maps. These

maps constitute an independent measure of the spatial variability of the instantaneous carbon fluxes and light absorption at the time of *HyPlant* overflight. BESS-GPP and APAR showed a nonlinear positive - even though scattered - correlation with F_{760} (r^2=0.46 and r^2=0.43, respectively). In addition, a positive nonlinear correlation was found between Fy_{760} and LUE (r^2=0.19). This result showed that this relationship, usually observed in the temporal domain, can hold in the spatial domain at the scale of individual tree crowns. At the same time, it entailed the need of taking into account the spatial variability, since it revealed that the relationship between F and GPP can be more complex at more detailed scale. BESS-GPP, -APAR and -LUE were also compared against F in the red region, showing more unexpected results. No significant correlation was in fact found between F_{687} and GPP or APAR, while a negative correlation was observed between Fy_{687} and LUE (r^2=0.25).

Jointly, our results provided insights into the critical role of the spatial heterogeneity in controlling the carbon fluxes, highlighting the importance of using high spatial resolution RS data to grasp the complexity of the terrestrial ecosystem dynamics. Furthermore, they pointed out the need to integrate different RS derived products to obtain a comprehensive picture of the vegetation related processes. Further research in this direction constitutes a high priority for advancing the understanding of terrestrial ecosystem dynamics and prediction of their future responses to a changing climate.

6. Acknowledgements

The data presented in this work were acquired in the framework of the SEN2ExpFL ("Technical Assistance for the Deployment of an advanced hyperspectral imaging sensor during SEN2ExpFL") and SEN2Exp ("Technical Assistance to fieldwork in the Hardt forest during SEN2Exp") projects funded by the European Space Agency (ESA Contract No 400011267/14/NL/BJ/lf and No 4000107143/12/NL/FF/lf).

The authors gratefully acknowledge the ground measurement team: M. Celesti, T. Julitta, C. Cilia, F. Fava, M. Weiss, B. Bes, N. Leroy, N. Breda, F. Bonne and F. Geremia.

M. Rossini, M. Migliavacca, U. Rascher and C. Panigada received funding from the European Union's Horizon 2020 research and innovation programme under the Marie Sklodowska-Curie grant agreement No

721995. J. Verrelst was supported by the European Research Council (ERC) under the ERC-2017-STG SENTIFLEX project (grant agreement No 755617).

7. References

Atzberger, C 2000, 'Development of an invertible forest reflectance model: The INFORM-Model', in Buchroithner (ed.), *Proceedings of the 20th EARSeL Symposium: A decade of trans-European Remote Sensing Cooperation, 14-16 June 2000, Dresden (Germany)*, pp. 39–44.

Atzberger, C & Richter, K 2012, 'Spatially constrained inversion of radiative transfer models for improved LAI mapping from future Sentinel-2 imagery', *Remote Sensing of Environment*, vol. 120, Elsevier Inc., pp. 208–218.

Atzberger, C, Darvishzadeh, R, Immitzer, M, Schlerf, M, Skidmore, AK & le Maire, G 2015, 'Comparative analysis of different retrieval methods for mapping grassland leaf area index using airborne imaging spectroscopy', *International Journal of Applied Earth Observation and Geoinformation*, vol. 43, Elsevier B.V., pp. 19–31.

Baker, NR 2008, 'Chlorophyll Fluorescence: A Probe of Photosynthesis In Vivo', *Annual Review of Plant Biology*, vol. 59, no. 1, pp. 89–113.

Ball, JT 1988, 'An analysis of stomatal conductance', Ph.D. Thesis.

Banskota, A, Serbin, SP, Wynne, RH, Thomas, VA, Falkowski, MJ, Kayastha, N & Townsend, PA 2015, 'An LUT-Based Inversion of DART Model to Estimate Forest LAI from Hyperspectral Data', *IEEE Journal of Selected Topics in Applied Earth Observations and Remote Sensing*, vol. 8, no. 6, pp. 3147–3160.

Baret, F & Buis, S 2008, 'Estimating canopy characteristics from remote sensing observations: review of methods and associated problems', *Advances in Land Remote Sensing. New York, USA.*, pp. 173–201.

Beer, C, Reichstein, M, Tomelleri, E, Ciais, P, Jung, M, Carvalhais, N, Roedenbeck, C, Arain, MA, Baldocchi, DD, Bonan, GB, Bondeau, A, Cescatti, A, Lasslop, G, Lindroth, A, Lomas, M, Luyssaert, S, Margolis, HA, Oleson, KW, Roupsard, O, Veenendaal, E, Viovy, N, Williams, C, Woodward, FI & Papale, D 2010, 'Terrestrial Gross Carbon Dioxide Uptake: Global Distribution and Covariation with Climate', *Science*, vol. 329, no. August, pp. 834–839.

735 Butler, EE, Datta, A, Flores-Moreno, H, Chen, M, Wythers, KR, Fazayeli, F, Banerjee, A, Atkin, OK,
736 Kattge, J, Amiaud, B, Blonder, B, Boenisch, G, Bond-Lamberty, B, Brown, KA, Byun, C, Campetella, G,
737 Cerabolini, B EL, Cornelissen, JH, Craine, JM, Craven, D, de Vries, FT, Díaz, S, Domingues, TF, Forey, E,
738 González-Melo, A, Gross, N, Han, W, Hattingh, WN, Hickler, T, Jansen, S, Kramer, K, Kraft, NJ, Kurokawa,
739 H, Laughlin, DC, Meir, P, Minden, V, Niinemets, Ü, Onoda, Y, Peñuelas, J, Read, Q, Sack, L, Schamp, B,
740 Soudzilovskaia, NA, Spasojevic, MJ, Sosinski, E, Thornton, PE, Valladares, F, van Bodegom, PM, Williams,
741 M, Wirth, C & Reich, PB 2017, 'Mapping local and global variability in plant trait distributions', *Proceedings of*
742 *the National Academy of Sciences*, p. 201708984.
743 Cao, M & Woodward, FI 1998, 'Dynamic responses of terrestrial ecosystem carbon cycling to global
744 climate change', *Nature*, vol. 393, no. May, pp. 249–252.
745 Chen, JM & Leblanc, SG 1997, 'A Four-Scale Bidirectional Reflectance Model Based on Canopy
746 Architecture', *IEEE Transactions on Geoscience and Remote Sensing*, vol. 35, no. 5, pp. 1316–1337.
747 Chen, JM & Black, T 1992, 'Defining leaf area index for non-flat leaves', *Plant, Cell and Environment*, vol.
748 15, pp. 421–429.
749 Cheng, Y Ben, Middleton, EM, Zhang, Q, Huemmrich, KF, Campbell, PK, Corp, LA, Cook, BD, Kustas,
750 WP & Daughtry, CS 2013, 'Integrating solar induced fluorescence and the photochemical reflectance index
751 for estimating gross primary production in a cornfield', *Remote Sensing*, vol. 5, no. 12, pp. 6857–6879.
752 Ciais, P., C. Sabine, G. Bala, L. Bopp, V. Brovkin, J. Canadell, A. Chhabra, R. DeFries, J. Galloway, M.
753 Heimann, C. Jones, C. Le Quéré, R.B. Myneni, S. Piao and P. Thornton, 2013, 'Carbon and Other
754 Biogeochemical Cycles'. In: Climate Change 2013: The Physical Science Basis. Contribution of Working
755 Group I to the Fifth Assessment Report of the Intergovernmental Panel on Climate Change [Stocker, T.F., D.
756 Qin, G.-K. Plattner, M. Tignor, S.K. Allen, J. Boschung, A. Nauels, Y. Xia, V. Bex and P.M. Midgley (eds.)].
757 Cambridge University Press, Cambridge, United Kingdom and New York, NY, USA.
758 Cogliati, S, Verhoef, W, Kraft, S, Sabater, N, Alonso, L, Vicent, J, Moreno, J, Drusch, M & Colombo, R
759 2015, 'Retrieval of sun-induced fluorescence using advanced spectral fitting methods', *Remote Sensing of*
760 *Environment*, vol. 169, Elsevier Inc., pp. 344–357.

761 Cogliati, S, Colombo, R, Celesti, M, Tagliabue, G, Rascher, U, Schickling, A, Rademske, P, Alonso, L,
762 Sabater, N, Drusch, M, Schüttemeyer, D 2018, 'Retrieval of the fluorescence emission by atmospheric
763 forward modelling and spectral fitting', *Proceedings of the International Geoscience and Remote Sensing*
764 *Symposium 2018.*
765 Combal, B, Baret, F, Weiss, M, Trubuil, A, Macé, D, Pragnère, A, Myneni, R, Knyazikhin, Y & Wang, L
766 2002, 'Retrieval of canopy biophysical variables from bidirectional reflectance using prior information to
767 solve the ill-posed inverse problem', *Remote Sensing of Environment*, vol. 84, no. 1, pp. 1–15.
768 Croft, H, Chen, JM, Zhang, Y & Simic, A 2013, 'Modelling leaf chlorophyll content in broadleaf and
769 needle leaf canopies from ground, CASI, Landsat TM 5 and MERIS reflectance data', *Remote Sensing of*
770 *Environment*, vol. 133, Elsevier Inc., pp. 128–140.
771 Croft, H, Chen, JM, Zhang, Y, Simic, A, Noland, TL, Nesbitt, N & Arabian, J 2015, 'Evaluating leaf
772 chlorophyll content prediction from multispectral remote sensing data within a physically-based modelling
773 framework', *ISPRS Journal of Photogrammetry and Remote Sensing*, vol. 102, International Society for
774 Photogrammetry and Remote Sensing, Inc. (ISPRS), pp. 85–95.
775 Croft, H, Chen, JM, Luo, X, Barlett, P, Chen, B & Staeble, RM 2017, 'Leaf chlorophyll content as a proxy
776 for leaf photosynthetic capacity', *Global Change Biology*, pp. 1–12.
777 Damm, A, Guanter, L, Laurent, V, Schaepman, ME, Schickling, A & Rascher, U 2014, 'FLD-based retrieval
778 of sun-induced chlorophyll fluorescence from medium spectral resolution airborne spectroscopy data',
779 *Remote Sensing of Environment*, vol. 147, Elsevier Inc., pp. 256–266.
780 Damm, A, Guanter, L, Paul-Limoges, E, van der Tol, C, Hueni, A, Buchmann, N, Eugster, W, Ammann, C
781 & Schaepman, ME 2015, 'Far-red sun-induced chlorophyll fluorescence shows ecosystem-specific
782 relationships to gross primary production: An assessment based on observational and modeling
783 approaches', *Remote Sensing of Environment*, vol. 166, Elsevier Inc., pp. 91–105.
784 Darvishzadeh, R, Skidmore, AK, Schlerf, M & Atzberger, C 2008, 'Inversion of a radiative transfer model
785 for estimating vegetation LAI and chlorophyll in a heterogeneous grassland', *Remote Sensing of Environment*,
786 vol. 112, no. 5, pp. 2592–2604.

787 de Pury, D & Farquhar, G 1997, 'Simple scaling of photosynthesis from leaves to canopies without the
788 errors of big-leaf models', *Plant Cell and Environment*, vol. 20, pp. 537–557.
789 Dorigo, WA, Zurita-Milla, R, de Wit, A, Brazile, J, Singh, R & Schaepman, ME 2007, 'A review on
790 reflective remote sensing and data assimilation techniques for enhanced agroecosystem modeling',
791 *International Journal of Applied Earth Observation and Geoinformation*, vol. 9, no. 2, pp. 165–193.
792 Drusch, M, Moreno, J, Del Bello, U, Franco, R, Goulas, Y, Huth, A, Kraft, S, Middleton, EM, Miglietta, F,
793 Mohammed, G, Nedbal, L, Rascher, U, Schüttemeyer, D & Verhoef, W 2017, 'The FLuorescence EXplorer
794 mission concept - ESA's Earth Explorer 8', *IEEE Trans. Geosci. Remote Sens.*, vol. 55, no. 3, pp. 1273–1284.
795 Du, S, Liu, L, Liu, X & Hu, J 2017, 'Response of canopy solar-induced chlorophyll fluorescence to the
796 absorbed photosynthetically active radiation absorbed by chlorophyll', *Remote Sensing*, vol. 9, no. 9.
797 Feret, J-B, François, C, Asner, GP, Gitelson, AA, Martin, RE, Bidel, LP, Ustin, SL, le Maire, G &
798 Jacquemoud, S 2008, 'PROSPECT-4 and 5: Advances in the leaf optical properties model separating
799 photosynthetic pigments', *Remote Sensing of Environment*, vol. 112, no. 6, pp. 3030–3043.
800 Frankenberg, C, Pollock, R, Lee, RAM, Rosenberg, R, Blavier, J, Crisp, D, Dell, CWO, Osterman, GB,
801 Roehl, C, Wennberg, PO & Wunch, D 2015, 'The Orbiting Carbon Observatory (OCO-2): spectrometer
802 performance evaluation using pre-launch direct sun measurements', *Atmospheric Measurement Techniques*,
803 vol. 8, pp. 301–313.
804 Frankenberg, C, Fisher, JB, Worden, J, Badgley, G, Saatchi, SS, Lee, J-E, Toon, GC, Butz, A, Jung, M, Kuze,
805 A & Yokota, T 2011, 'New global observations of the terrestrial carbon cycle from GOSAT: Patterns of plant
806 fluorescence with gross primary productivity', *Geophysical Research Letters*, vol. 38, no. 17, pp. 1–6.
807 Friedlingstein, P, Meinshausen, M, Arora, VK, Jones, CD, Anav, A, Liddicoat, SK & Knutti, R 2014,
808 'Uncertainties in CMIP5 Climate Projections due to Carbon Cycle Feedbacks', *American Meteorological Society*,
809 pp. 511–526.
810 Gastellu-Etchegorry, J, Demarez, V, Pinel, V & Zagolski, F 1996, 'Modeling Radiative Transfer in
811 Heterogeneous 3-D Vegetation Canopies', *Remote Sensing of Environment*, vol. 156, no. July 1995, pp. 131–156.

812 Genty, B, Briantais, JM & Baker, NR 1989, 'The relationship between the quantum yield of photosynthetic
813 electron transport and quenching of chlorophyll fluorescence', *Biochimica et Biophysica Acta - General Subjects*,
814 vol. 990, Elsevier Science Publishers B.V. (Biomedical Division), no. 1, pp. 87–92.
815 Gitelson, A & Merzlyak, MN 1994, 'Spectral Reflectance Changes Associated with Autumn Senescence of
816 Aesculus hippocastanum L. and Acer platanoides L. Leaves. Spectral Features and Relation to Chlorophyll
817 Estimation', *Journal of Plant Physiology*, vol. 143, Gustav Fischer Verlag, Stuttgart, no. 3, pp. 286–292.
818 Goulas, Y, Fournier, A, Daumard, F, Champagne, S, Ounis, A, Marloie, O & Moya, I 2017, 'Gross Primary
819 Production of a Wheat Canopy Relates Stronger to Far Red Than to Red Solar-Induced Chlorophyll
820 Fluorescence', *Remote Sensing*, vol. 9, no. 1, p. 97.
821 Guanter, L, Frankenberg, C, Dudhia, A, Lewis, PE, Gómez-Dans, J, Kuze, A, Suto, H & Grainger, RG
822 2012, 'Retrieval and global assessment of terrestrial chlorophyll fluorescence from GOSAT space
823 measurements', *Remote Sensing of Environment*, vol. 121, Elsevier Inc., pp. 236–251.
824 Guanter, L, Zhang, Y, Jung, M, Joiner, J, Voigt, M, Berry, J, Frankenberg, C, Huete, AR, Zarco-Tejada, PJ,
825 Lee, J-E, Moran, MS, Ponce-Campos, G, Beer, C, Camps-Valls, G, Buchmann, N, Gianelle, D, Klumpp, K,
826 Cescatti, A, Baker, JM & Griffis, TJ 2014, 'Global and time-resolved monitoring of crop photosynthesis with
827 chlorophyll fluorescence', *Proceedings of the National Academy of Sciences of the United States of America*, vol.
828 111, no. 14, pp. E1327-33.
829 Haining, R 1980, 'Spatial autocorrelation problems', 3, 1-44.
830 Hamazaki, T, Kaneko, Y & Kuze, A 2004, 'Carbon dioxide monitoring from the GOSAT satellite', in
831 *Proceedings of the XXth ISPRS conference, Istanbul, Turkey, 12–23 July 2004*.
832 Heimann, M & Reichstein, M 2008, 'Terrestrial ecosystem carbon dynamics and climate feedbacks',
833 *Nature*, vol. 451, no. 7176, pp. 289–292.
834 Hernández-Clemente, R, Navarro-Cerrillo, RM & Zarco-Tejada, PJ 2014, 'Deriving Predictive
835 Relationships of Carotenoid Content at the Canopy Level in a Conifer Forest Using Hyperspectral Imagery
836 and Model Simulation', *IEEE Transactions on Geoscience and Remote Sensing*, vol. 52, no. 8, pp. 5206–5217.

837 Homolova, L, Malenovský, Z, Clevers, JG, García-Santos, G & Schaepman, ME 2013, 'Review of optical-
838 based remote sensing for plant trait mapping', *Ecological Complexity*, vol. 15, pp. 1–16.
839 Houborg, R, McCabe, M, Cescatti, A, Gao, F, Schull, MA & Gitelson, A 2015a, 'Joint leaf chlorophyll
840 content and leaf area index retrieval from Landsat data using a regularized model inversion system
841 (REGFLEC)', *Remote Sensing of Environment*, vol. 159, Elsevier Inc., pp. 203–221.
842 Houborg, R, Fisher, JB & Skidmore, AK 2015b, 'Advances in remote sensing of vegetation function and
843 traits', *International Journal of Applied Earth Observation and Geoinformation*, vol. 43, pp. 1–6.
844 Inoue, Y, Peñuelas, J, Miyata, A & Mano, M 2008, 'Normalized difference spectral indices for estimating
845 photosynthetic efficiency and capacity at a canopy scale derived from hyperspectral and CO2 flux
846 measurements in rice', *Remote Sensing of Environment*, vol. 112, pp. 156–172.
847 Jacquemoud, S & Baret, F 1990, 'PROSPECT: A model of leaf optical properties spectra', *Remote Sensing of*
848 *Environment*, vol. 34, no. 2, pp. 75–91.
849 Jiang, C & Ryu, Y 2016, 'Multi-scale evaluation of global gross primary productivity and
850 evapotranspiration products derived from Breathing Earth System Simulator (BESS)', *Remote Sensing of*
851 *Environment*, vol. 186, Elsevier Inc., pp. 528–547.
852 Joiner, J, Yoshida, Y, Vasilkov, A, Yoshida, Y, Corp, LA & Middleton, EM 2011, 'First observations of
853 global and seasonal terrestrial chlorophyll fluorescence from space', *Biogeosciences*, vol. 8, no. 3, pp. 637–651.
854 Jung, M, Vetter, M, Herold, M, Churkina, G, Reichstein, M, Zaehle, S, Ciais, P, Viovy, N, Bondeau, A,
855 Chen, Y, Trusilova, K, Feser, F & Heimann, M 2007, 'Uncertainties of modeling gross primary productivity
856 over Europe: A systematic study on the effects of using different drivers and terrestrial biosphere models',
857 *Global Biogeochemical Cycles*, vol. 21, pp. 1–12.
858 Jung, M, Reichstein, M, Margolis, HA, Cescatti, A, Richardson, AD, Arain, MA, Arneth, A, Bernhofer, C,
859 Bonal, D, Chen, J, Gianelle, D, Gobron, N, Kiely, G, Kutsch, W, Lasslop, G, Law, BE, Lindroth, A, Merbold, L,
860 Montagnani, L, Moors, EJ, Papale, D, Sottocornola, M, Vaccari, F & Williams, C 2011, 'Global patterns of
861 land-atmosphere fluxes of carbon dioxide, latent heat, and sensible heat derived from eddy covariance,

862 satellite, and meteorological observations', *Journal of Geophysical Research: Biogeosciences*, vol. 116, no. 3, pp. 1–
863 16.

864 Knorr, W 2000, 'Annual and interannual CO_2 exchanges of the terrestrial biosphere: process-based
865 simulations and uncertainties', *Global Ecology and Biogeography*, vol. 9, pp. 225–252.

866 Knyazikhin, Y, Schull, MA, Stenberg, P, Mottus, M, Rautiainen, M, Yang, Y, Marshak, A, Latorre
867 Carmona, P, Kaufmann, RK, Lewis, PE, Disney, MI, Vanderbilt, V, Davis, AB, Baret, F, Jacquemoud, S,
868 Lyapustin, A & Myneni, RB 2013, 'Hyperspectral remote sensing of foliar nitrogen content', *Proceedings of the*
869 *National Academy of Sciences*, vol. 110, no. 3, pp. 185–192.

870 Kobayashi, H & Iwabuchi, H 2008, 'A coupled 1-D atmosphere and 3-D canopy radiative transfer model
871 for canopy reflectance , light environment , and photosynthesis simulation in a heterogeneous landscape',
872 *Remote Sensing of Environment*, vol. 112, pp. 173–185.

873 Koffi, EN, Rayner, PJ, Norton, AJ, Frankenberg, C & Scholze, M 2015, 'Investigating the usefulness of
874 satellite-derived fluorescence data in inferring gross primary productivity within the carbon cycle data
875 assimilation system', *Biogeosciences*, vol. 12, no. 13, pp. 4067–4084.

876 Kötz, B, Baret, F, Poilvé, H & Hill, J 2005, 'Use of coupled canopy structure dynamic and radiative
877 transfer models to estimate biophysical canopy characteristics', *Remote Sensing of Environment*, vol. 95, no. 1,
878 pp. 115–124.

879 Kuusk A 1991, 'The Hot Spot Effect in Plant Canopy Reflectance', in Photon-Vegetation Interactions, pp.
880 139-159.

881 Lang, A & Yueqin, X 1986, 'Estimation of Leaf Area Index from transmission of direct sunlight in
882 discontinuous canopies', *Agricultural and Forest Meteorology*, vol. 37, pp. 229–243.

883 Leonenko, G, Los, SO & North, PR 2013, 'Statistical distances and their applications to biophysical
884 parameter estimation: Information measures, m-estimates, and minimum contrast methods', *Remote Sensing*,
885 vol. 5, no. 3, pp. 1355–1388.

886 Lewis, PE & Disney, MI 2007, 'Spectral invariants and scattering across multiple scales from within-leaf to
887 canopy', *Remote Sensing of Environment*, vol. 109, no. 2, pp. 196–206.

888 Li, X, Xiao, J & He, B 2018, 'Chlorophyll fluorescence observed by OCO-2 is strongly related to gross
889 primary productivity estimated from flux towers in temperate forests', *Remote Sensing of Environment*, vol.
890 204, Elsevier, no. October 2017, pp. 659–671.
891 Lichtenthaler, HK & Buschmann, C 2001, 'Chlorophylls and Carotenoids: Measurement and
892 Characterization by UV-VIS Spectroscopy', *Current Protocols in Food Analytical Chemistry*, vol. 4, no. 3, pp. 1–
893 8.
894 Liu, L, Liu, X, Hu, J & Guan, L 2017, 'Assessing the wavelength-dependent ability of solar-induced
895 chlorophyll fluorescence to estimate the GPP of winter wheat at the canopy level', *International Journal of*
896 *Remote Sensing*, vol. 38, Taylor & Francis, no. 15, pp. 4396–4417.
897 Liu, X, Guanter, L, Liu, L, Damm, A, Rascher, U, Peng, D, Du, S & Gastellu-etchegorry, J 2018,
898 'Downscaling of solar-induced chlorophyll fluorescence from canopy level to photosystem level using a
899 random forest model', *Remote Sensing of Environment*, no. 9. (*in press*)
900 Malenovský, Z, Albrechtová, J, Lhotáková, Z, Zurita-Milla, R, Clevers, JG, Schaepman, ME & Cudlín, P
901 2006, 'Applicability of the PROSPECT model for Norway spruce needles', *International Journal of Remote*
902 *Sensing*, vol. 27, no. 24, pp. 5315–5340.
903 Malenovský, Z, Homolová, L, Zurita-Milla, R, Lukeš, P, Kaplan, V, Hanuš, J, Gastellu-Etchegorry, JP &
904 Schaepman, ME 2013, 'Retrieval of spruce leaf chlorophyll content from airborne image data using
905 continuum removal and radiative transfer', *Remote Sensing of Environment*, vol. 131, pp. 85–102.
906 Meroni, M, Colombo, R & Panigada, C 2004, 'Inversion of a radiative transfer model with hyperspectral
907 observations for LAI mapping in poplar plantations', *Remote Sensing of Environment*, vol. 92, no. 2, pp. 195–
908 206.
909 Meroni, M & Colombo, R 2009, '3S: A novel program for field spectroscopy', *Computers and Geosciences*,
910 vol. 35, Elsevier, no. 7, pp. 1491–1496.
911 Meroni, M, Busetto, L, Colombo, R, Guanter, L, Moreno, J & Verhoef, W 2010, 'Performance of Spectral
912 Fitting Methods for vegetation fluorescence quantification', *Remote Sensing of Environment*, vol. 114, Elsevier
913 Inc., no. 2, pp. 363–374.

914 Meroni, M, Barducci, A, Cogliati, S, Castagnoli, F, Rossini, M, Busetto, L, Migliavacca, M, Cremonese, E,
915 Galvagno, M, Colombo, R & Morra Di Cella, U 2011, 'The hyperspectral irradiometer, a new instrument for
916 long-term and unattended field spectroscopy measurements', *Review of Scientific Instruments*, vol. 82, pp. 1–
917 10.
918 Miao, G, Guan, K, Yang, X, Bernacchi, CJ, Berry, JA, DeLucia, EH, Wu, J, Moore, CE, Meacham, K, Cai, Y,
919 Peng, B, Kimm, H & Masters, MD 2018, 'Sun-Induced Chlorophyll Fluorescence, Photosynthesis, and Light
920 Use Efficiency of a Soybean Field from Seasonally Continuous Measurements', *Journal of Geophysical Research:*
921 *Biogeosciences*, vol. 123, no. 2, pp. 610–623.
922 Munro, R, Lang, R, Klaes, D, Poli, G, Retscher, C, Lindstrot, R, Huckle, R, Lacan, A, Grzegorski, M,
923 Holdak, A, Kokhanovsky, A, Livschitz, J & Eisinger, M 2016, 'The GOME-2 instrument on the Metop series
924 of satellites: instrument design, calibration, and level 1 data processing - an overview', *Atmospheric*
925 *Measurement Techniques*, vol. 9, pp. 1279–1301.
926 Omari, K, White, HP, Staenz, K & King, DJ 2013, 'Retrieval of Forest Canopy Parameters by Inversion of
927 the PROFLAIR Leaf-Canopy Re fl ectance Model Using the LUT Approach', *IEEE Journal of Selected Topics in*
928 *Applied Earth Observations and Remote Sensing*, vol. 6, no. 2, pp. 715–723.
929 Papageorgiou, GC & Govindjee, G 2004, in 'Chlorophyll Fluorescence: A Signature of Photosynthesis',
930 Kluwer Academic Publishers, pp. 1–42.
931 Paw, KT & Gao, W 1988, 'Applications of solutions to non-linear energy budget equations', *Agricultural*
932 *and Forest Meteorology*, vol. 43, pp. 121–145.
933 Porcar-Castell, A, Tyystjärvi, E, Atherton, J, Van Der Tol, C, Flexas, J, Pfündel, EE, Moreno, J,
934 Frankenberg, C & Berry, JA 2014, 'Linking chlorophyll a fluorescence to photosynthesis for remote sensing
935 applications: Mechanisms and challenges', *Journal of Experimental Botany*, vol. 65, no. 15, pp. 4065–4095.
936 Rascher, U, Alonso, L, Burkart, A, Cilia, C, Cogliati, S, Colombo, R, Damm, A, Drusch, M, Guanter, L,
937 Hanuš, J, Hyvarinen, T, Julitta, T, Jussila, J, Kataja, K, Kokkalis, P, Kraft, S, Kraska, T, Matveeva, M, Moreno,
938 J, Muller, O, Panigada, C, Pikl, M, Pinto, F, Prey, L, Pude, R, Rossini, M, Schickling, A, Schurr, U,

939 Schüttemeyer, D, Verrelst, J & Zemek, F 2015, 'Sun-induced fluorescence - a new probe of photosynthesis:
940 First maps from the imaging spectrometer HyPlant', *Global Change Biology*, vol. 21, no. 12, pp. 4673–4684.
941 Richter, K, Atzberger, C, Vuolo, F, Weihs, P & D'Urso, G 2009, 'Experimental assessment of the Sentinel-2
942 band setting for RTM-based LAI retrieval of sugar beet and maize', *Can. J. Remote Sensing*, vol. 35, no. 3, pp.
943 230–247.
944 Rivera, JP, Verrelst, J, Leonenko, G & Moreno, J 2013, 'Multiple cost functions and regularization options
945 for improved retrieval of leaf chlorophyll content and LAI through inversion of the PROSAIL model', *Remote*
946 *Sensing*, vol. 5, no. 7, pp. 3280–3304.
947 Rogers, A, Medlyn, BE, Dukes, JS, Bonan, GB, von Caemmerer, S, Dietze, MC, Kattge, J, Leakey, AD,
948 Mercado, LM, Niinemets, Ü, Colin Prentice, I, Serbin, SP, Sitch, S, Way, DA & Zaehle, S 2017, 'A roadmap for
949 improving the representation of photosynthesis in Earth system models', *New Phytologist*, vol. 213, no. 22–42.
950 Rosema, A, Verhoef, W, Noorbergen, H & Borgesius, J 1992, 'A new forest light interaction model in
951 support of forest monitoring', *Remote Sensing of Environment*, vol. 42, no. 1, pp. 23–41.
952 Rossini, M, Meroni, M, Migliavacca, M, Manca, G, Cogliati, S, Busetto, L, Picchi, V, Cescatti, A, Seufert, G
953 & Colombo, R 2010, 'High resolution field spectroscopy measurements for estimating gross ecosystem
954 production in a rice field', *Agricultural and Forest Meteorology*, vol. 150, Elsevier B.V., no. 9, pp. 1283–1296.
955 Rouse, J, Haas, J & Deering, D 1974, 'Monitoring vegetation systems in the Great Plains with ERTS', in
956 *Third Earth Resources Technology Satellite-1 Symposium - Volume I: Technical Presentations. Washington D.C.*
957 *NASA*, pp. 309–317.
958 Ryu, Y, Baldocchi, DD, Kobayashi, H, Van Ingen, C, Li, J, Black, TA, Beringer, J, Van Gorsel, E, Knohl, A,
959 Law, BE & Roupsard, O 2011, 'Integration of MODIS land and atmosphere products with a coupled-process
960 model to estimate gross primary productivity and evapotranspiration from 1 km to global scales', *Global*
961 *Biogeochemical Cycles*, vol. 25, no. 4, pp. 1–24.
962 Ryu, Y, Jiang, C, Kobayashi, H & Detto, M 2018, 'MODIS-derived global land products of shortwave
963 radiation and di ff use and total photosynthetically active radiation at 5 km resolution from 2000', *Remote*
964 *Sensing of Environment*, vol. 204, Elsevier, no. September 2017, pp. 812–825.

965 Schimel, DS 1995, 'Terrestrial ecosystems and the carbon cycle', *Global Change Biology*, no. October 1994,
966 pp. 77–91.
967 Schimel, DS, Pavlick, R, Fisher, JB, Asner, GP, Saatchi, S, Townsend, P & Miller, C 2015, 'Observing
968 terrestrial ecosystems and the carbon cycle from space', *Global Change Biology*, vol. 21, pp. 1762–1776.
969 Schlerf, M & Atzberger, C 2006, 'Inversion of a forest reflectance model to estimate structural canopy
970 variables from hyperspectral remote sensing data', *Remote Sensing of Environment*, vol. 100, no. 3, pp. 281–
971 294.
972 Schlerf, M & Atzberger, C 2012, 'Vegetation structure retrieval in beech and spruce forests using
973 spectrodirectional satellite data', *IEEE Journal of Selected Topics in Applied Earth Observations and Remote*
974 *Sensing*, vol. 5, no. 1, pp. 8–17.
975 Sun, Y, Frankenberg, C, Wood, JD, Schimel, DS, Jung, M, Guanter, L, Drewry, DT, Verma, M, Porcar-
976 Castell, A, Griffis, TJ, Gu, L, Magney, T, Köhler, P, Evans, B & Yuen, K 2017, 'OCO-2 advances
977 photosynthesis observation from space via solar-induced chlorophyll fluorescence', *Science*, vol. 358, no.
978 6360.
979 Tagliabue, G, Panigada, C, Colombo, R, Fava, F, Cilia, C, Baret, F, Vreys, K, Meuleman, K & Rossini, M
980 2016, 'Forest species mapping using airborne hyperspectral APEX data', *Miscellanea Geographica, Regional*
981 *Studies on Development*, vol. 20, no. 1, pp. 1–6.
982 Tramontana, G, Jung, M, Schwalm, CR, Ichii, K, Camps-Valls, G, Ráduly, B, Reichstein, M, Arain, MA,
983 Cescatti, A, Kiely, G, Merbold, L, Serrano-Ortiz, P, Sickert, S, Wolf, S & Papale, D 2016, 'Predicting carbon
984 dioxide and energy fluxes across global FLUXNET sites with regression algorithms', *Biogeosciences*, vol. 13,
985 no. 14, pp. 4291–4313.
986 van Bodegom, PM, Douma, JC, Witte, J, Ordoñez, J, Bartholomeus, R & Aerts, R 2012, 'Going beyond
987 limitations of plant functional types when predicting global ecosystem-atmosphere fluxes: Exploring the
988 merits of traits-based approaches', *Global Ecology and Biogeography*, vol. 21, no. 6, pp. 625–636.
989 van Bodegom, PM, Douma, JC & Verheijen, LM 2014, 'A fully traits-based approach to modeling global
990 vegetation distribution', *Proceedings of the National Academy of Sciences*, vol. 111, no. 38, pp. 13733–13738.

van der Tol, C, Verhoef, W, Timmermans, J, Verhoef, A & Su, Z 2009, 'An integrated model of soil-canopy spectral radiances, photosynthesis, fluorescence, temperature and energy balance', *Biogeosciences*, vol. 6, no. 12, pp. 3109–3129.

van der Tol, C, Berry, JA, Campbell, PK & Rascher, U 2014, 'Models of fluorescence and photosynthesis for interpreting measurements of solar-induced chlorophyll fluorescence', Journal of Geophysical Research: *Biogeosciences*, vol. 119, no. 12, pp. 2312–2327.

Verhoef, W 1984, 'Light scattering by leaf layers with application to canopy reflectance modeling: The SAIL model', *Remote Sensing of Environment*, vol. 16, no. 2, pp. 125–141.

Verhoef, W, van der Tol, C & Middleton, EM 2018, 'Hyperspectral radiative transfer modeling to explore the combined retrieval of biophysical parameters and canopy fluorescence from FLEX - Sentinel-3 tandem mission multi-sensor data', *Remote Sensing of Environment*, vol. 204, Elsevier, no. October 2017, pp. 942–963.

Verma, M, Schimel, DS, Evans, B, Frankenberg, C, Beringer, J, Drewry, DT, Magney, T, Marang, I, Hutley, L, Moore, CE & Eldering, A 2017, 'Effect of environmental conditions on the relationship between solar-induced fluorescence and gross primary productivity at an OzFlux grassland site', *Journal of Geophysical Research: Biogeosciences*, vol. 122, no. 3, pp. 716–733.

Verrelst, J, Rivera, JP, Alonso, L & Moreno, J 2011, 'ARTMO: an automated radiative transfer models operator toolbox for automated retrieval of biophysical parameters through model inversion', in *Proceedings of 7th EARSeL Workshop on Imaging Spectrometry, Edinburgh, UK, 11-13 April 2011*.

Verrelst, J, Rivera, JP, Leonenko, G, Alonso, L & Moreno, J 2014, 'Optimizing LUT-based RTM inversion for semiautomatic mapping of crop biophysical parameters from Sentinel-2 and -3 data: Role of cost functions', *IEEE Transactions on Geoscience and Remote Sensing*, vol. 52, no. 1, pp. 257–269.

Verrelst, J, Camps-Valls, G, Muñoz-Marí, J, Rivera, JP, Veroustraete, F, Clevers, JG & Moreno, J 2015a, 'Optical remote sensing and the retrieval of terrestrial vegetation bio-geophysical properties - A review', *ISPRS Journal of Photogrammetry and Remote Sensing*, vol. 108, International Society for Photogrammetry and Remote Sensing, Inc. (ISPRS), pp. 273–290.

1016 Verrelst, J, Rivera, JP, Veroustraete, F, Muñoz-Marí, J, Clevers, JG, Camps-Valls, G & Moreno, J 2015b,
1017 'Experimental Sentinel-2 LAI estimation using parametric, non-parametric and physical retrieval methods -
1018 A comparison', *ISPRS Journal of Photogrammetry and Remote Sensing*, vol. 108, International Society for
1019 Photogrammetry and Remote Sensing, Inc. (ISPRS), pp. 260–272.
1020 Verrelst, J, Rivera, JP, Moreno, J 2015c, 'ARTMO's global sensitivity analysis (GSA) toolbox to quantify
1021 driving variables of leaf and canopy radiative transfer models'. *EARSeL eProceedings*, Special Issue 2:
1022 9th EARSeL Imaging Spectroscopy Workshop, 2015. 1-11.
1023 Verrelst, J, Rivera, JP, van der Tol, C, Magnani, F, Mohammed, GH & Moreno, J 2015d, 'Global sensitivity
1024 analysis of the SCOPE model: What drives simulated canopy-leaving sun-induced fluorescence?', *Remote*
1025 *Sensing of Environment*, vol. 166, Elsevier Inc., pp. 8–21.
1026 Verrelst, J, van der Tol, C, Magnani, F, Sabater, N, Rivera, JP, Mohammed, GH & Moreno, J 2016,
1027 'Evaluating the predictive power of sun-induced chlorophyll fluorescence to estimate net photosynthesis of
1028 vegetation canopies: A SCOPE modeling study', *Remote Sensing of Environment*, vol. 176, Elsevier Inc., pp.
1029 139–151.
1030 Verrelst, J, Malenovský, Z, van der Tol, C, Camps-Valls, G, Gastellu-Etchegorry, JP, Lewis, P, North, P &
1031 Moreno, J 2018, 'Quantifying Vegetation Biophysical Variables from Imaging Spectroscopy Data: A Review
1032 on Retrieval Methods', *Surveys in Geophysics*, Springer Netherlands, pp. 1–41.
1033 Wang, Z, Skidmore, AK, Darvishzadeh, R & Wang, T 2018, 'Mapping forest canopy nitrogen content by
1034 inversion of coupled leaf-canopy radiative transfer models from airborne hyperspectral imagery',
1035 *Agricultural and Forest Meteorology*, vol. 253–254, Elsevier, no. January, pp. 247–260.
1036 White, HP, Miller, JR & Chen, JM 2001, 'Four-Scale Linear Model for Anisotropic Reflectance (FLAIR) for
1037 Plant Canopies - Part I: Model Description and Partial Validation', *IEEE Transactions on Geoscience and Remote*
1038 *Sensing*, vol. 39, no. 5, pp. 1072–1083.
1039 Whitley, R, Beringer, J, Hutley, LB, Abramowitz, G, Kauwe, MG De, Duursma, R, Evans, B, Haverd, V, Li,
1040 L, Ryu, Y, Smith, B, Wang, Y-P, Williams, M & Yu, Q 2016, 'A model inter-comparison study to examine
1041 limiting factors in modelling Australian tropical savannas', *Biogeosciences*, vol. 13, pp. 3245–3265.

1042 Wieneke, S, Ahrends, HE, Damm, A, Pinto, F, Stadler, A, Rossini, M & Rascher, U 2016, 'Airborne based
1043 spectroscopy of red and far-red sun-induced chlorophyll fluorescence: Implications for improved estimates
1044 of gross primary productivity', *Remote Sensing of Environment*, vol. 184, Elsevier B.V., pp. 654–667.
1045 Wohlfahrt, G & Gu, L 2015, 'The many meanings of gross photosynthesis and their implication for
1046 photosynthesis research from leaf to globe', *Plant Cell and Environment*, vol. 38, no. 12, pp. 2500–2507.
1047 Yang, G, Zhao, C, Liu, Q, Huang, W & Wang, J 2011, 'Inversion of a radiative transfer model for
1048 estimating forest LAI from multisource and multiangular optical remote sensing data', Geoscience and
1049 Remote Sensing, IEEE Transactions on, vol. 49, no. 3, pp. 988–1000.
1050 Yang, X, Tang, J, Mustard, JF, Lee, J, Rossini, M, Joiner, J, Munger, WJ, Kornfeld, A & Richardson, AD
1051 2015, 'Solar-induced chlorophyll fluorescence correlates with canopy photosynthesis on diurnal and seasonal
1052 scales in a temperate deciduous forest', Geophysical Research Letters, pp. 2977–2987.
1053 Yang, K, Ryu, Y, Dechant, B, Berry, JA, Hwang, Y, Jiang, C, Kang, M, Kim, J, Kimm, H, Kornfeld, A &
1054 Yang, X 2018, 'Sun-induced chlorophyll fluorescence is more strongly related to absorbed light than to
1055 photosynthesis at half-hourly resolution in a rice paddy', *Remote Sensing of Environment*, vol. 216, Elsevier,
1056 no. June, pp. 658–673.
1057 Zarco-Tejada, PJ, Miller, JR, Morales, A, Berjón, A & Agüera, J 2004, 'Hyperspectral indices and model
1058 simulation for chlorophyll estimation in open-canopy tree crops', Remote Sensing of Environment, vol. 90,
1059 no. 4, pp. 463–476.
1060 Zhang, Y, Guanter, L, Berry, JA, van der Tol, C, Yang, X, Tang, J & Zhang, F 2016, 'Model-based analysis
1061 of the relationship between sun-induced chlorophyll fluorescence and gross primary production for remote
1062 sensing applications', *Remote Sensing of Environment*, vol. 187, Elsevier Inc., pp. 145–155.
1063 Zhu, Z, Piao, S, Myneni, RB, Huang, M, Zeng, Z, Canadell, JG, Ciais, P, Sitch, S, Friedlingstein, P, Arneth,
1064 A, Liu, R, Mao, J, Pan, Y, Peng, S, Peñuelas, J & Poulter, B 2016, 'Greening of the Earth and its drivers',
1065 *Nature Climate Change*, vol. 6, no. April, pp. 791–796.